

Supplementary Materials

A beginner's guide to low-coverage whole genome sequencing for population genomics

Runyang Nicolas Lou^{1*}, Arne Jacobs^{1,2}, Aryn Wilder³, Nina O. Therkildsen^{1*}

¹Department of Natural Resources and the Environment, Cornell University, Ithaca, NY 14853, USA

²Current address: Institute of Biodiversity, Animal Health and Comparative Medicine, University of Glasgow, Glasgow, G12 8QQ, UK

³San Diego Zoo Wildlife Alliance, Escondido, CA 92027, USA

*Corresponding authors: RNL (rl683@cornell.edu), NOT (nt246@cornell.edu)

TABLE OF CONTENTS

Supplementary methods	5
Section 2: Estimation of the cost of lcWGS	5
Section 4: Population genomic inference from lcWGS data under different experimental designs	6
Section 5: Analysis of down-sampled <i>Heliconius</i> data	11
Box 4: Using imputation to bolster genotype estimation from lcWGS	12
Sensitivity of population genomic inference power to simulation assumptions	15
Additional details on software packages for the analysis of low-coverage data	16
References for software in Table 2 of the main text	19
Supplementary tables	20
Table S1. List of population genomics studies using lcWGS.	20
Table S2. Model parameters used for forward genetic simulation.	22
Table S3. <i>Heliconius erato</i> short read archive (SRA) IDs. Individuals used for the subsampling and genotype-likelihood-based analysis of <i>H. erato</i> subspecies, with SRA ID and subspecies names. Samples from (Van Belleghem et al., 2017).	22
Supplementary figures	25
Figure S1. Histogram of the allele frequencies of false negative SNPs with lcWGS. Across the different facets, sample size increases from left to right, and coverage increases from top to bottom. The total sequencing effort remains the same along the diagonal from bottom left to top right.	25
Figure S2. Distribution of Tajima's θ (aka π) and Watterson's θ estimated using the Samtools genotype likelihood model and the GATK genotype likelihood model in 10kb windows. Across the different facets, sample size increases from left to right, and coverage increases from top to bottom. The total sequencing effort remains the same	

44 along the diagonal from bottom left to top right. The true chromosome-average values for
45 both statistics should be 0.004, which is marked with a red line. 26

46 **Figure S3.** Tajima's D estimated using the Samtools genotype likelihood model and the
47 GATK genotype likelihood model in 10kb windows. Across the different facets, sample
48 size increases from left to right, and coverage increases from top to bottom. The total
49 sequencing effort remains the same along the diagonal from bottom left to top right. The
50 true chromosome-average Tajima's D should be 0, which is marked with a red line. 27

51 **Figure S4.** Linkage disequilibrium (LD) estimated using ngsLD from simulated data. LD,
52 shown on the y axis, is measured as r^2 between pairs of SNPs, and the physical
53 distance between these SNP pairs is shown on the x axis. The blue line shows the mean
54 of the estimated r^2 for each distance value, and the lighter blue area shows its
55 interquartile range. The red line marks the theoretical expectation of r^2 under mutation-
56 drift equilibrium. Across the different facets, sample size increases from left to right, and
57 coverage increases from top to bottom. The total sequencing effort remains the same
58 along the diagonal from bottom left to top right. 28

59 **Figure S5.** Estimated linkage disequilibrium (LD) fitted to a linkage decay model using
60 ngsLD. The solid blue line shows the best fitted model, and the dashed blue lines
61 represent its 95% confidence interval. When the true recombination rate is known, the
62 effective population size (N_e) can be calculated from the estimated LD decay rate and is
63 shown on the top right corner in each facet. The true effective population size used in the
64 simulation is 100,000. The red line marks the theoretical expectation of r^2 under
65 mutation-drift equilibrium, given by ref. Across the different facets, sample size increases
66 from left to right, and coverage increases from top to bottom. The total sequencing effort
67 remains the same along the diagonal from bottom left to top right. 29

68 **Figure S6.** The sequencing coverage distribution that we sampled from when simulating
69 uneven sequencing coverage among samples. This distribution is obtained by merging
70 the distributions of coverage among samples from three of our lcWGS projects where we
71 pooled samples by molarity. 30

72 **Figure S7.** The error in allele frequency estimation with lcWGS (yellow) and Pool-seq
73 (blue) data, both with uneven coverage among individual samples. The distribution of
74 absolute errors ($|\text{estimated frequency} - \text{true frequency}|$) is shown with the box plots along
75 the x-axis. The lower and upper hinges of the box plots show 25th and 75th percentile of
76 the absolute errors, and the whiskers extend to the largest or smallest values no further
77 than 1.5 times the interquartile range. Outlier points are hidden. Across the different
78 facets, sample size increases from left to right, and coverage increases from top to
79 bottom. The total sequencing effort remains the same along the diagonal from bottom left
80 to top right. The root mean squared error (RMSE) for the two sequencing designs are
81 shown in each facet. False negative SNPs are not included in this figure. See
82 supplementary methods and Figure S7 for how uneven coverage was simulated. 31

83 **Figure S8.** An empirical example from one of our lcWGS projects of the distribution of
84 raw sequencing yield from individual samples when they are repooled based on the first
85 round of sequencing. This is to demonstrate that equal distribution of sequencing effort
86 can be approximated by such a sequencing design. (The type specimens were designed
87 to have higher sequencing yield than other samples.) 32

88 **Figure S9.** The spatial population structures inferred through principal component
89 analysis (PCA) with lcWGS data using PCA. The first two principal components are
90 shown. This result is from our higher gene flow scenario (an average of 1 effective
91 migrant from one population to another every generation), but a longer chromosome is
92 simulated (300Mbp, or 10 times longer than the scenarios shown in Figure 4). Sample
93 size remains five per sample, and coverage increases from top to bottom. 33

94 **Figure S10.** Patterns of spatial population structure inferred through principal component
95 analysis (PCA) with lcWGS data using PCAngsd, in a scenario with lower gene flow (an
96 average of 0.25 effective migrants per generation). Sample size per population increases

97 across panels from left to right, and coverage per sample increases from top to bottom.
98 This figure is based on the same dataset as Figure 5A, in which case ANGSD was used
99 instead of PCAngsd to perform the PCA. 34

100 **Figure S11.** Patterns of spatial population structure inferred through principal component
101 analysis (PCA) with lcWGS data using PCAngsd, in a scenario with higher gene flow (an
102 average of 1 effective migrants per generation). Sample size per population increases
103 across panels from left to right, and coverage per sample increases from top to bottom.
104 This figure is based on the same dataset as Figure 5B, in which case ANGSD was used
105 instead of PCAngsd to perform the PCA. 35

106 **Figure S12.** The true per-SNP F_{ST} values along the chromosome between the two
107 simulated populations in a scenario with smaller N_e ($N_e = 104$) and lower gene flow (an
108 average of 2.5 effective migrants from one population to the other every generation).
109 Neutral SNPs are shown in black and selected SNPs are shown in black. 36

110 **Figure S13.** Genome-wide scan for divergent selection with lcWGS data in a scenario
111 with smaller N_e ($N_e = 104$) and lower gene flow (an average of 2.5 effective migrants
112 from one population to the other every generation). The F_{ST} values inferred from lcWGS
113 data in 5kb windows along the chromosome are shown on the y axis. Sample size
114 increases from left to right, and coverage increases from top to bottom. The black points
115 mark both the selected and neutral SNPs, and the red asterisks only mark the positions
116 of the selected SNPs (not their inferred F_{st} values). 37

117 **Figure S14.** Genome-wide scan for divergent selection with RADseq data in a scenario
118 with smaller N_e ($N_e = 104$) and lower gene flow (an average of 2.5 effective migrants
119 from one population to the other every generation). The per-SNP F_{ST} values inferred
120 from RAD-seq data are shown on the y axis and the SNP positions are shown on the x
121 axis. Sample size increases from left to right, and RAD-tag density increases from top to
122 bottom. The black points mark both the selected and neutral SNPs, and the red asterisks
123 only mark the positions of the selected SNPs (not their inferred F_{st} values). 38

124 **Figure S15.** Principal components plot and estimates of genetic differentiation around
125 the optix gene for the Heliconius dataset at 4x (top) and 1x coverage (bottom),
126 respectively. 39

127 **Figure S16.** Genotype estimation accuracy (r^2) by minor allele frequency (MAF) for
128 imputation in STITCH and Beagle compared to posterior genotypes estimated without
129 imputation. Combinations of sample size (n ; with increasing n indicated by more
130 contiguous lines) and sequencing coverage (plots in rows correspond to 1x, 2x and 4x
131 coverage) were tested for each method (line colors) under different diversity and linkage
132 disequilibrium scenarios. Note the different y-axis scales. 40

133 **Figure S17.** Genotype concordance by minor allele frequency (MAF) for imputation in
134 STITCH and Beagle and without imputation. Genotypes were called with minimum
135 posterior genotype probability of 0.9. Combinations of sample size (n ; with increasing n
136 indicated by more contiguous lines) and sequencing coverage (plots in rows correspond
137 to 1x, 2x and 4x coverage) were tested for each method (line colors) under different
138 diversity and linkage disequilibrium scenarios. Note the different y-axis scales. 41

139 **Figure S18.** Proportion of genotypes called by minor allele frequency (MAF) for
140 imputation in STITCH and Beagle and without imputation. Genotypes were called with
141 minimum posterior genotype probability of 0.9. Combinations of sample size (n ; with
142 increasing n indicated by more contiguous lines) and sequencing coverage (plots in rows
143 correspond to 1x, 2x and 4x coverage) were tested for each method (line colors) under
144 different diversity and linkage disequilibrium scenarios. Note the different y-axis scales.
145 42

146 **Figure S19.** Genotype estimation by imputation in STITCH and Beagle compared to
147 posterior genotypes estimated without imputation for sites with $MAF > 0.05$. Combinations
148 of sample size (n ; with increasing n indicated by more contiguous lines) and sequencing
149 coverage (x-axis) were tested for each method (line colors) under different diversity and

150 linkage disequilibrium scenarios. (A)-(C) Mean r^2 between true genotypes and estimated
151 genotype dosage. (D)-(F) Genotype concordance (GC) between true and called
152 genotypes with posterior genotype probability >0.9 . G-I) Proportion of genotypes called
153 with posterior genotype probability >0.9 . 43

154 **Figure S20.** Change in accuracy (r^2) of minor allele frequencies (MAF) estimation using
155 imputed genotype probabilities from STITCH and Beagle, relative to non-imputed
156 genotype likelihoods. Values above the x-axis show r^2 for MAF estimated without
157 imputation. The three diversity/LD scenarios are arranged in columns, sample sizes
158 ($n=100, 250, 500$ and 1000) are arranged in rows, and sequencing depths are shown on
159 the x-axis. Note the different y-axis scales. 44

160 **Supplementary References** 45

161

162

163

164 **Supplementary methods**

165

166 Section 2: Estimation of the cost of lcWGS

167 The cost estimates presented in Table 1 assume a per library cost of 8 USD (details in
168 Therkildsen and Palumbi 2017). This is the pro-rated cost of the reagents needed for a
169 single library. An important consideration for researchers adopting lcWGS for the first time,
170 is that many of the reagents needed are only available in relatively large batches, requiring a
171 substantial upfront investment. One of the most expensive reagents to acquire is often a
172 sufficiently large set of indexed (barcoded) adapter oligos needed to individually label each
173 library. To avoid misassigned reads due to index hopping, we recommend a unique dual
174 index strategy (i.e. two unique oligos per sample for the P5 and P7 ends of the library
175 construct (MacConaill et al., 2018)). With November 2020 pricing, custom synthesis of each
176 adapter oligo pair would cost ~44 USD, bringing the initial investment for oligos for 50
177 uniquely barcoded samples (which can then be pooled in a single sequencing lane) to
178 ~2,200 USD. Several commercial barcoding adapter kits are also available and may be a
179 cheaper option if a relatively small total number of samples are to be processed. The
180 investment in indexed adapters is for most users a one-time investment in a resource that
181 can split among laboratories.

182

183

184

185 Section 4: Population genomic inference from lcWGS data under different experimental
186 designs

187

188 In short, we used SLiM3 (Haller & Messer, 2019) to generate forward genetic simulations of
189 a 30Mbp chromosome within *in silico* populations under a diploid Wright-Fisher model. The
190 simulated populations had an effective population size (N_e) of 10^5 (unless otherwise noted),
191 a mutation rate of 10^{-8} per base per generation, and a recombination rate of 2.5 cM/Mbp.
192 These parameters were set to resemble a typical metazoan species with a relatively large
193 population size (Allio, Donega, Galtier, & Nabholz, 2017; Stapley, Feulner, Johnston,
194 Santure, & Smadja, 2017), and see a discussion of how different parameter choices can
195 affect our results in the supplementary materials). We then sampled a subset of individuals
196 in these populations and used ART-MountRainier (Huang, Li, Myers, & Marth, 2012) to
197 simulate different lcWGS experimental designs with different combinations of sample size
198 and coverage per sample. We performed genotype-likelihood-based analyses of these
199 simulated sequencing reads with ANGSD, and tested the power of different experimental
200 designs in population genetic inference. We used the Samtools genotype likelihood model
201 implemented in ANGSD (-GL 1) and only report the results from GATK model (-GL 2) when
202 the two show significant discrepancies. In addition, we simulated other high-throughput
203 sequencing strategies, including Pool-seq and RAD-seq, and compared their performance
204 with that of lcWGS (detailed methods in the supplementary materials).

205

206 To examine the performance for different types of population genomic inference, we
207 generated three separate sets of simulations. First, we simulated an isolated population to
208 test the accuracy of lcWGS in estimating key population genetic parameters in a single
209 population. Second, we simulated two different metapopulations to test the ability of lcWGS
210 to infer spatial structure among subpopulations under different levels of connectivity. Lastly,
211 we simulated two populations closely connected by gene flow under divergent selection, and
212 tested the power of lcWGS to identify the genetic loci under selection. The key model
213 parameters used in our simulations are summarized in Table S2, and our entire simulation
214 and analysis pipeline is available on GitHub (<https://github.com/therkildsen-lab/lcwgssimulation>).
215

216

217 **Population genomic inference for single populations:** First, we tested the accuracy of
218 low-coverage sequencing in allele frequency estimation with different sequencing strategies
219 in a single simulated population with stable population size and no selection. We used
220 SLiM3 (Haller & Messer, 2019) to randomly generate a starting nucleotide sequence on a
221 30Mbp chromosome, and then created a diploid population with all individuals initially having
222 this same starting sequence. We aimed to simulate a large population with effective
223 population size (N_e) on the order of 10^5 . However, it is computationally expensive to directly
224 simulate large population sizes with forward genetic simulation methods, since all individuals
225 in the population need to be tracked in every generation, and more time is required to reach
226 mutation-drift equilibrium. Therefore, we chose to scale down our simulated population size
227 (N) by a factor of 100, and scale up the mutation rate (μ) and recombination rate (r) by a
228 factor of 100. Because the most important parameters of the simulated population (e.g.
229 nucleotide diversity, linkage disequilibrium, site frequency spectrum) depends on products in
230 the form of $N\mu$, Nr , and etc., this scaling approach can generate a realistic population with a
231 reasonable computational cost. Specifically, we set N to be 1,000, and ran the simulation
232 with $\mu = 1 \times 10^{-6}$ per bp per generation and $r = 250$ cM/Mbp for 10,000 generations, resulting

233 in a population that has achieved mutation-drift equilibrium with population genetic
234 parameters similar to what we find in natural diploid animal populations with N_e on the order
235 of 10^5 (Allio et al., 2017; Stapley et al., 2017). All mutations are neutral in this simulation. We
236 outputted the entire haplotype sequences at the last generation in fasta format. We also
237 output the true allele frequency for each site. Next, for each haplotype sequence, we used
238 ART-MountRainier (W. Huang et al., 2012) to simulate the sequencing process on an
239 Illumina platform with 150-base paired-end reads and 10x coverage for each haplotype. We
240 then sorted the resulting bam files and merged the two bam files originating from the two
241 haplotypes of each individual. We selected a combination of sample size (5, 10, 20, 40, 60,
242 80, 160) and coverage per sample (0.25x, 0.5x, 1x, 2x, 4x, 8x) by randomly subsampling
243 these merged bam files. For each of these different combinations of sample size and
244 coverage, we called SNPs and performed genotype likelihoods (using the Samtools
245 genotype likelihood model) and allele frequency estimation using ANGSD-0.931 with the
246 following options `-GL 1 -doGlf 2 -doMaf 1 -doMajorMinor 5 -doCounts 1 -doDepth 1 -dumpCounts 3`
247 `-SNP_pval 1e-6 -rmTriallelic 1e-6 -setMinDepth 2 -minInd 1 -minMaf 0.0005 -minQ 20`. We were
248 then able to compare the inferred allele frequencies with the true allele frequencies in the
249 simulated population, and quantify the accuracy in allele frequency estimation by calculating
250 the Coefficient of determination (R^2) and root-mean-square error (RMSE) using custom R
251 scripts (Figure 2). We also estimated the sample allele frequency likelihoods (SAF) and
252 subsequently the site frequency spectrum (SFS) using ANGSD. For SAF, we found that a
253 more stringent depth filter has better performance, so we used the following options `-doSaf 1`
254 `-GL 1 -doCounts 1 -setMinDepth sample_size*coverage`. For SFS, we found that extending the
255 number of iterations can improve its performance, and thus run the realSFS module in
256 ANGSD with the following options `-tole 1e-08 -maxIter 1000`. From the estimated SFS, we
257 calculated different estimators of theta (e.g. Watterson's estimator, Tajima's estimator) and
258 performed neutrality tests (e.g. Tajima's D) in 10kb windows, using ANGSD with the
259 following options: `-GL 1 -doSaf 1 -doThetas 1 -doCounts 1 -setMinDepth sample_size*coverage`,
260 and the thetaStat module in ANGSD with the following options: `do_stat -win 10000 -step 10000`
261 (Figure S2, S3). To compare the performance between different genotype likelihood models,
262 we replicated the entire analysis pipeline above using the GATK genotype likelihood model
263 (`-GL 2`) (Figure S2, S3). Lastly, from the genotype likelihoods calculated using the Samtools
264 model, we estimated linkage disequilibrium (LD) between intermediate frequency SNPs
265 (minimum minor allele frequency = 0.1) within 5kb of each other using ngsLD (Fox et al.
266 2019) with the following options: `--probs --rnd_sample 1 --max_kb_dist 5 --min_maf 0.1` (Figure
267 S4). We then fitted the estimated r^2 values with the LD decay model described by Hill and
268 Weir (1988) using the `fit_LDdecay.R` script in ngsLD with the following options: `--fit_level 2 --`
269 `n_ind $SAMPLE_SIZE --fit_boot 1000` (Figure S5). We also computed the theoretical
270 expectation of LD decay curve using the effective population size and recombination rate
271 used in our simulation, also based on the model described by Hill and Weir (1988) (Figure
272 S4, S5).

273
274 **Inference of spatial structure:** Then, we tested the power of low-coverage sequencing in
275 resolving the genetic structure of spatially distributed populations. Again, we began by
276 randomly creating a starting sequence on a 30Mbp chromosome, but this time we created
277 nine populations, each with N of 500. These nine populations are distributed on a three-by-
278 three grid, with a constant bidirectional migration rate (m) equal to 0.0005 (or 0.002 in the
279 high migration rate scenario) connecting each pair of adjacent populations (Figure 4).
280 Similarly, we scaled up the neutral mutation rate (μ) to 2×10^{-7} per bp per generation, and

281 recombination rate (r) to 50cM/Mbp. We ran the simulation for 10,000 generations, resulting
282 in a metapopulation that has achieved mutation-drift-migration equilibrium. This
283 metapopulation consists of nine populations, each with population genetic parameters
284 resembling a diploid animal population with effective population size (N_e) on the order of
285 10^4 . We used ART to simulate the sequencing process, and subsampled the bam files to
286 create different combinations of sample size (5, 10, 20, 40, 60, 80) and coverage per sample
287 (0.125x, 0.25x, 0.5x, 1x, 2x, 4x). We called SNPs and estimated genotype likelihoods with
288 the nine populations combined using `-GL 1 -doGlf 2 -doMaf 1 -doMajorMinor 5 -doCounts 1 -`
289 `doDepth 1 -dumpCounts 1 -doIBS 2 -makematrix 1 -doCov 1 -P 6 -SNP_pval 1e-6 -rmTriallelic 1e-6 -`
290 `setMinDepth 2 -minInd 1 -minMaf 0.05 -minQ 20` in ANGSD. This step outputs a covariance
291 matrix (`-doCov 1`) and a distance matrix (`-doIBS 2`) among individuals, and in addition to
292 these, we also used PCAngsd (Meisner & Albrechtsen, 2018) to generate another
293 covariance matrix using the estimated genotype likelihoods. Using the `eigen()` function and
294 the `cmdscale()` function in R, we conducted principal component analysis (PCA) and principal
295 coordinate analysis (PCoA) with these covariances matrices and distance matrix,
296 respectively, plotted the samples on the first two principal components / principal
297 coordinates, and compared these with the true spatial structure that was simulated (Figure
298 4, S10, S11). Also, we performed PCA with the true sample genotypes using PLINK2 as an
299 additional comparison (Figure 4). Lastly, to test whether performance improves with
300 genome-wide data instead of a single chromosome, we simulated a longer chromosome of
301 300Mbp under the high migration rate scenario, and repeated the entire pipeline but only
302 with 5 samples per population (Figure S9).

303

304 **Scans for divergent selection in the face of gene flow:** Lastly, we tested the power of
305 low-coverage sequencing in detecting signatures of divergent selection between two
306 populations connected by gene flow. This simulation consists of two stages: a neutral burn-
307 in stage, and a selection stage. Two populations under mutation-drift-migration equilibrium
308 are created in the burn-in stage, and then selection is imposed on these populations in the
309 selection stage. In the burn-in stage, we began by randomly creating a starting sequence on
310 a 30Mbp chromosome and two populations, each with a population size (N) of 500, and with
311 a constant bidirectional migration rate (m) between them. We used a scaled-up
312 recombination rate (r) and neutral mutation rate (μ), ran the simulation for 5,000 generations,
313 and outputted the entire populations. In the first generation of the selection stage, we read
314 the output from the burn-in stage into SLiM, selected 11 evenly distributed positions on the
315 chromosome, and at each of these positions we added a non-neutral mutation to one
316 randomly sampled genome in the first population. These mutations were set to be beneficial
317 in the first population with a certain selection coefficient (s) and deleterious in the second
318 population with a selection coefficient of ($1/s$). Despite this, since these non-neutral
319 mutations each exist in a single copy, a majority of them are likely to get lost in the first few
320 generations of the selection due to drift, in which case the simulation needs to be reset. To
321 avoid resetting the simulation too many times (which can take a long time), we instantly
322 expanded the population size by a factor of 10 (to 5,000) in each population after introducing
323 the non-neutral mutations, which would then exist in multiple copies. Correspondingly, we
324 scaled down the original m , r , and μ by a factor of 10, in order to preserve the key population
325 genomic parameters of the simulated populations. We ran the simulation for an additional
326 200 generations. If more than half of the selected alleles become lost due to drift or Hill-
327 Robertson interference during the process, we restart from the beginning of the selection
328 stage with a different random seed (the same burn-in is always used). After the selection

329 stage is complete, the SNP density is mainly determined by the mutation rate (μ), the
330 background level of differentiation between the two populations is mainly determined by the
331 migration rate (m), the level of differentiation at the selected locus is mainly determined by
332 both the selection coefficient (s) and the migration rate (m), and the width of the genomic
333 region that shows high differentiation between the two populations is mainly determined by
334 the recombination rate (r). We were therefore able to create population pairs with different
335 genomic landscapes of differentiation by reiterating this process with different combinations
336 of mutation rate (μ), selection coefficients (s), migration rates (m), and recombination rates
337 (r) (Table S2). Then, we again subsampled each population, and used ART to simulate the
338 sequencing process with the same combinations of sample size (5, 10, 20, 40, 60, 80, 160)
339 and coverage per sample (0.25x, 0.5x, 1x, 2x, 4x, 8x) as in our neutral model. Using
340 ANGSD, we called SNPs with the two populations combined through `-dosaf 1 -GL 1 -doGlf 2 -`
341 `doMaf 1 -doMajorMinor 5 -doCounts 1 -doDepth 1 -dumpCounts 1 -SNP_pval 1e-6 -rmTriallelic 1e-6 -`
342 `setMinDepth 2 -minInd 1 -minMaf 0.0005 -minQ 20`, estimated genotype likelihoods and allele
343 frequencies for each population through `-dosaf 1 -GL 1 -doGlf 2 -doMaf 1 -doMajorMinor 5 -`
344 `doCounts 1 -doDepth 1 -dumpCounts 1 -setMinDepth 1 -minInd 1 -minQ 20`, and finally estimated
345 per-SNP F_{st} between the population pair from the two-dimensional site frequency spectrum
346 estimated from realSFS using the default option. Using custom R scripts, we visualized and
347 compared the F_{st} landscape under different simulation scenarios and sequencing strategies
348 (Figure 5, S12, S13).

349
350 **Comparison with Pool-seq:** In addition to these investigations on different sequencing
351 designs of low-coverage whole genome sequencing, we have also compared low-coverage
352 whole genome sequencing with two other commonly used high-throughput sequencing
353 strategies, namely pool-seq and RAD-seq. With pool-seq, we were mainly interested in its
354 accuracy in allele frequency estimation (in comparison to the estimation with individually
355 barcoded low-coverage samples), particularly when the sequencing yield from different
356 individuals in the pool is uneven, which is avoidable with a lcWGS design by repooling
357 (Figure S6) but is almost inevitable with pool-seq. Therefore, we simulated pool-seq with our
358 neutral model under two different scenarios. In the first scenario, we assumed that the
359 sequencing yield is equal among individuals. In this case, the simulation and analysis is
360 exactly the same as in low-coverage whole genome sequencing until the last step, where
361 instead of using the allele frequency estimates outputted by ANGSD, we calculated allele
362 frequencies based on the allele counts in the population instead (this was generated by `-`
363 `minQ 20 -doCounts 1 -dumpCounts 1`) (Figure 3). In the second scenario, we kept the total
364 sequencing yield to be the same, but added variation in the contribution of each individual to
365 the pool. To do this, we sampled each individual's sequencing yield from an empirical
366 distribution, which we obtained by subsampling and rescaling the individual sequencing yield
367 from three of our low-coverage whole genome sequencing projects where we tried our best
368 effort to generate even yield among samples by pooling by DNA molarity. These empirical
369 sequencing yields have a right-skewed distribution with a standard deviation that
370 is 60% of the mean (Figure S7). We subsampled each individual bam file according to its
371 target yield, and inputted these subsampled bam files to the same ANGSD pipeline for SNP
372 calling, genotype likelihoods estimation, and allele frequency estimation. Allele frequency
373 estimates outputted by the pipeline would represent the result from low-coverage whole
374 genome sequencing, and allele frequencies calculated from allele counts would represent
375 the estimates from pool-seq. We again calculated R^2 and RMSE from these allele frequency
376 estimates as a measure of their accuracy (Figure S8).

377
378
379
380
381
382
383
384
385
386
387
388
389
390

Comparison with RAD-seq: With RAD-seq, we were mainly interested in its power in identifying genomic islands of differentiation. Therefore, we simulated RAD-seq with our divergent selection model. We assumed that with the high coverage of RAD-seq, genotypes can always be called correctly, so we used true genotypes instead of simulating the sequencing process. We used R to randomly sample 150-bp fragments on our 30MB genome as our RAD tags at a range of different densities (4, 8, 16, 32, 64, and 128 per MB), obtained each sample's true genotype at these fragments, and calculated sample allele frequencies. We used these allele frequencies to estimate per-SNP F_{st} ($F_{st} = 1 - H_S / H_T$), visualized and then compared these F_{st} results with those from low-coverage whole genome sequencing simulation (Figure 6, S14).

391 Section 5: Analysis of down-sampled *Heliconius* data

392

393 To determine the effect of sequencing coverage on our ability to detect local signatures of
394 differentiation and global population structure we re-analysed *Heliconius spp.* whole-genome
395 data from (Van Belleghem et al., 2017). Raw whole-genome data for 70 *H. erato* individuals
396 were downloaded from NCBI (Supplementary Table S3) and mapped to the *H. erato*
397 demophoon reference genome (*Heliconius_erato_demophoon_v1*) using BOWTIE2
398 (Langmead & Salzberg, 2013) using the --very-sensitive setting. Reads with mapping
399 qualities (MAPQ) below 20 were filtered out and the remaining reads sorted using
400 SAMTOOLS v.1.9 (Heng Li et al., 2009). Duplicated reads were removed using
401 MARKDUPLICATES v.2.9.0 from PICARD TOOLS and reads realigned around indels using
402 PICARD.

403

404 Subsequently, we subsampled each filtered bam file based on the fraction of reads to an
405 approximated coverage of 8x (30M reads per individual), 4x (15M reads), 2x (7.5M reads),
406 1x(3.75M reads) and 0.5x(1.625M reads) using SAMTOOLS. Individuals with insufficient
407 coverage for a mean of 8x were filtered out (2 individuals).

408

409 To determine how the ability to detect local signatures of differentiation differs with coverage,
410 we estimated F_{st} between individuals with red-bar and no red-bar along the genomic
411 scaffold containing the underlying gene *optix* (scaffold Herato1801:) (Van Belleghem et al.,
412 2017). Individuals with the same phenotypes were pooled across sampling sites and
413 subspecies to achieve sample sizes of 23 red-barred individuals (*H. e. demophoon*, *H. e.*
414 *favorinus*; *H. e. hydara* and *H. e. notabilis*) and 28 non-barred individuals (*H. e. amalfreda*,
415 *H. e. emma*; *H. e. erato*; *H. e. lativitta* and *H. e. etylus*). Using each set of subsampled bam
416 file, we identified variant sites across scaffold Herato1801 using ANGSD v.0.28 with the
417 following criteria: SNP_p-val=1e-6; minDepth = Number of individuals * 0.1x; maxDepth =
418 coverage * N.ind + (2 * coverage * N.ind); minInd=75% of individuals (= 40); minQ = 30; and
419 minMAF=0.05 (Korneliussen, Albrechtsen, & Nielsen, 2014). F_{st} values were estimated
420 based on these variant sites (-sites option) in ANGSD based on genotype likelihoods in 50kb
421 sliding windows with a 20kb step size to make them comparable to results in (Van
422 Belleghem et al., 2017).

423

424 To understand how the sequencing coverage affects the ability to detect global population
425 structure in *Heliconius*, we performed a principal components analysis for all individuals at
426 each coverage based on covariance matrices estimated in ANGSD. Covariance matrices
427 were estimated using a random-read sampling procedure in ANGSD and PCA was
428 performed using the eigen function in R. All results were plotted in R using ggplot.

429

430

431

432 Box 4: Using imputation to bolster genotype estimation from lcWGS

433

434 **Simulations:** To explore imputation performance under different scenarios, we used the
435 same forward simulation framework as in section 4.1 to simulate a 30MB chromosome for
436 three neutrally evolving populations that have reached mutation-drift equilibrium. We set the
437 mutation rate (μ) to be 1×10^{-8} /bp/generation for all three populations, and altered their
438 effective population size (N_e) and recombination rate (r), creating three different scenarios
439 with different levels of genetic diversity and linkage disequilibrium (LD). Genetic diversity and
440 LD are known to affect imputation performance (Pasaniuc et al., 2012). In a neutral
441 population, genetic diversity is proportional to the product of effective population size and
442 mutation rate, whereas LD is inversely proportional to the product of effective population size
443 and recombination rate, and accordingly, our three scenarios were characterized by 1) a low
444 diversity, high LD scenario ($r = 0.5$ cM/Mbp, $N_e = 1,000$); 2) a medium diversity, medium LD
445 scenario ($r = 0.5$ cM/Mbp, $N_e = 10,000$); and 3) a medium diversity, low LD scenario ($r = 2.5$,
446 $N_e = 10,000$).

447 We generated sample sizes of 25, 100, 250, 500 or 1000 individuals from a single,
448 neutrally evolving population of stable size for each simulated scenario. We sampled with
449 replacement $2n$ haplotypes (n diploid individuals) from the offspring of the final generation of
450 the simulation. Similar to our approach in Section 4, we used ART-MountRainier (W. Huang
451 et al., 2012) to simulate bam files of sequence reads to average depths of 1x, 2x and 4x per
452 individual for each sample size, for a total of five sample sizes x three depths x three
453 population scenarios = 45 datasets.

454

455 **SNP calling and genotype estimation with and without imputation:** For each dataset,
456 we evaluated the accuracy of genotype dosages and genotypes called using imputation
457 without a reference panel in the programs Beagle v.3.3.2 and STITCH v.3.6.2. For
458 comparison, we called genotypes and estimated genotype dosages without imputation in
459 ANGSD v.0.931. (Although ANGSD recommends basing downstream analyses on genotype
460 likelihoods rather than called genotypes, we use it as a baseline for evaluating any
461 improvement of genotype calls by imputation.) For all downstream analyses, we first
462 identified SNPs in ANGSD using the settings (-GL 1 -doGlf 2 -doMaf 1 -doMajorMinor 5 -
463 doCounts 1 -doDepth 1 -dumpCounts 3 -P 6 -SNP_pval 1e-6 -rmTriallelic 1e-6 -setMinDepth
464 2 -minInd 1 -minMaf 0.0005 -minQ 20).

465 We called non-imputed genotypes directly from the posterior genotype probability in
466 ANGSD, using minor allele frequencies as a prior and a posterior probability cutoff of 0.90 (-
467 postCutoff 0.90 -doPost 1 -doMaf 1 -GL 2 -dogeno 5 -doMajorMinor 3). Because ANGSD
468 does not directly output genotype dosages, we converted posterior genotype probabilities
469 using the formula genotype dosage = $P(AA | \text{data}) * 0 + P(AB | \text{data}) * 1 + P(BB | \text{data}) * 2$.

470 Before running the full imputation in STITCH, we explored performance under
471 varying settings of the parameter K ($K=25, 30$ and 35), and examined output plots as well as
472 r^2 values between simulated genotypes and imputation dosages. In most cases $K=30$
473 performed best or very close to best; thus, we used the settings $K=30$, $n\text{Gen}=10$, and $S=4$,
474 and called genotypes with posterior probability ≥ 0.90 . For the imputation in Beagle, we
475 passed genotype likelihoods estimated in ANGSD directly to Beagle and ran the imputation
476 under default settings. We called genotypes from posterior genotype probability threshold of
477 0.9 using the script `gprobs2beagle.jar`
478 (https://faculty.washington.edu/browning/beagle_utilities/utilities.html).

479 We evaluated the performance of each method in the following ways, by the proportion
480 of correct genotype calls (genotype concordance), the proportion of genotypes actually
481 called, and by the r^2 between allelic dosage and true genotypes within allele frequency bins
482 of size 0.05. We report average values for all sites with $MAF > 0.05$, excluding variant sites
483 that were not identified (false negatives) or non-variant sites called as SNPs (false positives)
484 in the ANGSD SNP-calling step.

485

486 **Genotype calling rates and genotype concordance with imputation:** At the smallest
487 sample size tested ($n=25$), there was little to no improvement in accuracy using Beagle, and
488 accuracy actually decreased when imputation was performed in STITCH with 25 samples
489 (Figures S16-S18), suggesting that such small sample sizes are inadequate for reliable
490 imputation; thus we focused our results on $n \geq 100$. For all sample sizes and sequencing
491 depths across scenarios, the accuracy of genotype estimates varied with allele frequency.
492 The correlation (r^2) between imputed allelic dosage and true genotypes was low for sites
493 with minor allele frequency ($MAF < 0.05$ to 0.10), but increased and was relatively consistent
494 across higher MAF bins (Figure S16). Genotype concordance (GC), by contrast, had the
495 opposite relationship with MAF ; GC was higher for sites with low MAF and decreased with
496 higher MAF (Figure S16). This is because it is easy to achieve high accuracy by calling the
497 homozygous major genotype when the minor allele is rare. In order to summarize overall
498 imputation performance, we averaged r^2 , GC and the proportion of called genotypes across
499 sites with $MAF > 0.05$ for each combination of method, scenario and study design (Figure
500 S16-18).

501 Genotype concordance (GC) was universally high for all methods and sequencing
502 strategies ($GC > 0.9$), except for imputation of 100 samples from the medium diversity, high
503 LD scenario in STITCH (Figure S19D-F). At 1x coverage, fewer than half of genotypes were
504 called by Beagle and without imputation, especially for sites with higher MAF (Figure S18).
505 GC was similar under the medium diversity, medium LD scenario compared to the low
506 diversity, high LD scenario (Figure S19D-E), except GC was somewhat lower for genotypes
507 imputed in STITCH at 1x coverage. The least improvement in GC using imputation was seen
508 under medium diversity, low LD scenario (Figure S19F). For $n \leq 250$ samples sequenced at
509 1x and 2x coverage, GC for genotypes imputed in STITCH were less accurate than those
510 estimated without imputation.

511 Overall, imputation accuracy required larger sample sizes or was reduced altogether
512 as genetic diversity and recombination rates increased. This was particularly true for the
513 program STITCH, which estimates distinct haplotype probabilities within a given region
514 across a mosaic of ancestral haplotypes (Davies, Flint, Myers, & Mott, 2016), a problem that
515 becomes increasingly complex under high recombination. Imputation showed larger
516 improvements with increasing sample size in STITCH than in Beagle, especially at low
517 coverage (1x), whereas Beagle improved more with increasing sequence read depth (Figure
518 9).

519

520 **Allele frequency estimation from imputed genotype probabilities:** Because imputation
521 increased the accuracy of posterior genotype probabilities under most of the tested
522 scenarios and study designs, we asked whether allele frequency estimation was improved
523 by using imputed genotype probabilities compared to MAF estimation without imputation. To
524 estimate MAF from imputed genotype probabilities, we summed over the posterior genotype
525 probabilities (-domaf 4 in ANGSD), and compared the results to MAF estimated from
526 genotype likelihoods using the EM algorithm implemented in ANGSD (-domaf 1). Under

527 some scenarios and study designs, imputation resulted in small improvements in accuracy
528 of allele frequency estimation (Figure S20). Imputation yielded the largest improvements in
529 allele frequency estimation for large sample sizes ($N \geq 250$) sequenced at 1x coverage from
530 the low diversity, high LD population, and from the medium diversity, medium LD population.
531 For small sample sizes from the medium diversity, low LD population, MAF estimated from
532 genotype probabilities imputed in STITCH were less accurate. Beagle showed more
533 consistent, modest improvements, increasing MAF estimation accuracy when coverage was
534 $\geq 2x$ for all sample sizes and scenarios.

535 Under the low diversity, high LD scenario, allele frequency estimates based on
536 genotype probabilities imputed in STITCH from 1000 samples at 1x coverage were slightly
537 more accurate ($r^2=0.999$) than for 500 samples at 2x coverage ($r^2=0.998$) and 250 samples
538 at 4x coverage ($r^2=0.997$). However, given that smaller sample sizes are already sufficient
539 for estimating allele frequencies with high accuracy without imputation ($r^2=0.990$ for MAF
540 estimated from 250 samples sequenced at 1x coverage; Figure S20), imputation is not likely
541 to contribute to analyses of these types of population-level statistics as much as it would for
542 individual-level and genotype-level analyses like GWAS.

543

544

545

546 **Sensitivity of population genomic inference power to simulation assumptions**

547

548 In Section 4 of this paper, we have tested the performance of different types of population
549 genomic inference under different lcWGS experimental designs using forward genetic
550 simulation. We found that for most of these analyses, distributing the same amount of
551 sequencing effort across more samples can consistently improve inference power. This
552 conclusion should be relatively robust regardless of the parameter settings in our simulation
553 model, although the power of inference under each combination of sample size and
554 coverage can be strongly affected by these model assumptions. Here, we briefly present a
555 qualitative discussion on how the power of different types of population genomic inference
556 could be impacted by different parameter choices in the simulation.

557

558 **Section 4.1:** Given the same true allele frequency, the accuracy of allele frequency
559 estimation at a single SNP should be largely independent of simulation parameters other
560 than sample size and coverage. The values of RMSE and r^2 genome-wide, however, will be
561 sensitive to the site frequency spectrum (SFS) in the simulated data, since errors are
562 strongly affected by the true allele frequencies (Figure 2). As a result, any processes that
563 can skew the SFS (e.g. demographic expansion and contraction, selection) could affect the
564 values of RMSE and r^2 , although the directionality of the change is context dependent.

565

566 **Section 4.2:** For the inference of spatial structure, higher migration rate is an obvious driver
567 for lower inference power (Figure 4). We have also shown that with more SNPs (which can
568 result from a larger genome, larger population size, or higher mutation rate), inference power
569 can improve (Figure S9). On the other hand, stronger LD (caused by lower population size
570 or lower recombination rate) should decrease the power of inference, since SNPs can
571 become highly correlated with each other, resulting in fewer independent SNPs that are
572 informative.

573

574 **Section 4.3:** Similarly, a larger number of SNPs in the dataset due to higher mutation rate
575 can also lead to higher power to locate the region under divergent selection, as a window-
576 based approach can have more information to work with. Stronger LD due to lower
577 recombination rate generates more distinct patterns of linked selection, therefore also
578 enhances the power to locate the general region of interest. Both factors, however, have a
579 more complex effect on the power to locate the causal SNPs due to the higher number of
580 linked neutral SNPs that potentially become false positives. Stronger divergent selection
581 should be able to more reliably increase the detection power of both the general region of
582 interest and the causal SNPs. Lastly, the effects of population size and migration rate is also
583 complex. On the one hand, higher population size leads to more SNPs in the dataset. On
584 the other hand, it can result in narrower peaks that are more difficult to detect due to
585 reduced LD. Lower migration rate increases the F_{st} values of the selected SNPs, but also
586 increases the background noise. A more quantitative power analysis is therefore warranted
587 to better understand the effect of these simulation parameters.

588

589

590 **Additional details on software packages for the analysis of low-coverage data**

591

592 In this section, we include some additional details about the software packages that we
593 introduced in Section 4 of the main text. When applicable, we highlight the methodological
594 differences between the different packages for solving the same problem.

595

596 **Genotype likelihood models:** Four different genotype likelihood models are currently
597 implemented in ANGSD. The GATK model (McKenna et al., 2010) assumes that base
598 quality scores at the same site from different sequencing reads are each an independent
599 and unbiased representation of the probabilities of sequencing error, whereas the Samtools
600 model (Li, 2011) assumes that these quality scores are not completely independent. Both
601 the SYK model (Kim et al., 2011) and the SOAPsnp model (Li et al., 2009) assume that the
602 quality scores could be biased and thus implement a quality score recalibration step. In the
603 SKY mode, type specific error rates (e.g. the probability of an A being called a T) are
604 estimated and accounted for in GL calculation. In the SOAPsnp model, in addition to the
605 type specific errors, strand and read position specific errors can be accounted for as well,
606 but a set of invariant loci should be provided to minimize biases. Additional genotype
607 likelihood models are adopted by other software packages and they can be useful
608 alternatives to ANGSD for specific types of data. For example, the program Atlas
609 (Kousathanas et al., 2017) explicitly incorporates post-mortem DNA damage in addition to
610 sequencing error in its genotype likelihood model, making it well-suited for ancient DNA
611 studies. EBG (Blischak, Kubatko, & Wolfe, 2018) uses a simplified version of the SAMtools
612 model but relaxes ANGSD's assumption of diploidy, allowing the analysis of polyploid
613 samples.

614

615 **SNP identification:** In ANGSD, SNPs are inferred by first estimating allele frequencies at
616 each site (including the presumably invariable loci) and then testing whether its minor allele
617 frequency is significantly larger than zero (Korneliussen et al., 2014). Accordingly, the first
618 step is to restrict the number of alleles that can possibly occur at each site to two: a major
619 allele, and a minor allele. The identities of these alleles can be determined through a
620 maximum likelihood approach (Jørsboe & Albrechtsen, 2019; Skotte, Korneliussen, &
621 Albrechtsen, 2012) or by user specification. Next, the likelihood of the minor allele frequency
622 at each site can be formulated as a function of genotype likelihoods across all individuals
623 (see Equation 2 in (Kim et al., 2011)), and these minor allele frequencies can be estimated
624 using a maximum likelihood approach. In this way, all possible genotypes for each individual
625 can be considered, effectively avoiding explicitly calling genotypes. Then, polymorphic sites
626 will be identified through a likelihood ratio test (Kim et al., 2011). The list of polymorphic sites
627 (i.e. SNPs) can then be exported and used for downstream analyses, along with the
628 genotype likelihoods at each of these sites for each individual. Other software programs
629 address SNP calling in similar ways. Atlas, for example, follows the same general framework
630 as ANGSD, but has made modifications (Kousathanas et al., 2017) to accommodate cases
631 where the sample size is very small and neither the major nor the minor alleles is specified
632 by users, which is often the case for ancient DNA studies (Kousathanas et al., 2017).

633

634 **Dimensionality reduction methods for population structure inference:** The random
635 read sampling method employed by ANGSD does not take full advantage of the entire
636 dataset. In contrast, ngsTools (Fumagalli, Vieira, Linderroth, & Nielsen, 2014) uses a more
637 sophisticated method where posterior genotype probabilities are first calculated with an

638 empirical Bayes approach. This approach is valid under the assumption of Hardy-Weinberg
639 equilibrium across the entire sample set, but for most structured populations, this
640 assumption will not hold, which can lead to inaccurate PCA results (e.g. population clusters
641 can have long tails, see Meisner & Albrechtsen, 2018). PCAngsd (Meisner & Albrechtsen,
642 2018) therefore takes one step further and uses an iterative approach to correct for potential
643 violation of the HWE assumption by updating prior genotype probabilities based on the PCA
644 result in each previous iteration, since these PCA results can represent the population
645 structure that exists in the data (Meisner & Albrechtsen, 2018).

646
647 **Model-based clustering for population structure inference:** NGSAdmix (Skotte,
648 Korneliussen, & Albrechtsen, 2013) adopts a maximum likelihood implementation of the
649 classic STRUCTURE model (Tang, Peng, Wang, & Risch, 2005)(Pritchard, Stephens, &
650 Donnelly, 2000), (Tang et al., 2005), but formulates a likelihood function with sequencing
651 data as its observed data and uses genotype likelihoods to consider all possible genotypes
652 for each individual (see Equation 6 in Skotte et al., 2013). It then uses an expectation-
653 maximization (EM) algorithm to estimate model parameters. Because of the more complex
654 formulation of the likelihood function, however, NGSAdmix tends to be computationally
655 demanding. As an alternative, Ohana (Cheng, Racimo, & Nielsen, 2019) adopts the same
656 likelihood function as NGSAdmix but uses a sequential quadratic programming (QP) method
657 instead of EM for optimization, which should speed up computation. No formal comparison
658 between the performance of the two methods is available to date, but separate evaluations
659 on simulated and real data have shown that both methods deliver great accuracy even at
660 very low coverage (Cheng et al., 2019; Skotte et al., 2013). Distinct from both NGSAdmix
661 and Ohana, PCAngsd uses individual allele frequencies, an intermediate output from its
662 PCA analysis, as input for a non-negative matrix factorization (NMF) algorithm to infer
663 admixture proportions.

664
665 **Genome-wide association analysis:** In Kim et al. (2011), case / control association is
666 tested by first estimating allele frequencies within case and control individuals with the
667 approach as described in the “SNP identification” section, and then using a likelihood ratio
668 test for differences between case and control individuals at each locus (see equations 6-7 in
669 Kim et al. 2011). The first step in Skotte et al. (2012) and Jørsboe & Albrechtsen (2019) is to
670 calculate the posterior genotype probability using an empirical Bayes approach, with priors
671 informed by either population allele frequencies or the SFS. Skotte et al. (2012) then used a
672 score statistics approach to test for significant associations with the phenotype at each site.
673 This approach is computationally efficient, but cannot estimate the effect size of the loci. In
674 contrast, (Jørsboe & Albrechtsen, 2019) employs a maximum likelihood approach to
675 explicitly estimate the effect size of each locus. As expected, this approach is slower than
676 the score statistics method. To take advantage of both methods, ANGSD also implements a
677 hybrid approach, first using the score statistic to identify significant loci, and then using the
678 maximum-likelihood approach to estimate effect sizes of these significant loci.

679
680 **Linkage disequilibrium:** GUS-LD (Bilton et al., 2018) constructs a likelihood function of the
681 LD coefficient D and uses a numerical method to optimize the likelihood function. In contrast,
682 ngsLD (Fox, Wright, Fumagalli, & Vieira, 2019) constructs a likelihood function of the
683 haplotype frequencies between each pair of SNPs instead, and uses an EM algorithm to
684 optimize it (Fox et al., 2019). Different LD statistics, such as D , D' and r^2 , can then be

685 derived from the inferred haplotype frequencies. Furthermore, ngsLD incorporates several
686 other helpful features, such as LD pruning and the fitting of an LD decay model.

687

688 **Allele frequency estimation:** As mentioned in the SNP identification section, ANGSD takes
689 a maximum-likelihood approach to estimate allele frequencies among all samples (Kim et
690 al., 2011). It then uses the same algorithm to estimate the frequencies of the minor alleles in
691 each population separately for each site identified as polymorphic (based on the selected
692 filtering and confidence threshold). It is important to note that a SNP significance filter or a
693 minimum minor allele frequency filter should not be applied in population-specific allele
694 frequency estimation, because sites fixed for the major allele in a subset of populations
695 (which would be removed by these filters) are typically of interest. Other programs that can
696 estimate allele frequencies from genotype likelihoods follow the same general workflow.
697 Atlas (Kousathanas et al., 2017), for example, adopts a similar maximum likelihood
698 framework, but also provides a Bayesian inference option.

699

700 **Genetic diversity and neutrality test statistics within a single population:** To estimate θ
701 in different parts of the genome, ANGSD adopts an empirical Bayes approach, where the
702 SFS within a window (posterior) can be formulated and solved as the product of the SAF
703 likelihoods within the window (likelihood) and the genome-wide or chromosome-wide SFS
704 (prior) (see the equation in the “Empirical Bayes” section in Korneliussen, Moltke,
705 Albrechtsen, & Nielsen, 2013). Different θ estimators can then be extracted from the SFS in
706 each window.

707

708 **Genetic differentiation between populations:** ANGSD implements the method-of-moment
709 estimator of F_{ST} developed by (Reynolds, Weir, & Cockerham, 1983). While different
710 estimators of θ depend on the local SFS within a single population, Reynolds et al.’s
711 estimator of pairwise F_{ST} can be formulated as a function of the local two-dimensional SFS
712 (the matrix with the joint distribution of allele counts in two populations). Therefore, ANGSD
713 again takes an empirical Bayes approach, using the maximum likelihood method to estimate
714 a genome-wide two-dimensional SFS, which it then uses as a prior to calculate the two-
715 dimensional SFS at each genomic locus. F_{ST} at each locus can then be derived from these
716 locus-specific SFS. GPAT (<http://www.yandell-lab.org/software/gpat.html>) implements two
717 additional methods to estimate F_{ST} using genotype likelihoods as its input. In the first method
718 (wc F_{ST}), GPAT estimates allele frequencies from genotype likelihoods and directly plugs the
719 estimated allele frequencies into Weir and Cockerham's F_{ST} estimator. This method is
720 computationally efficient but may not account for the uncertainties in the estimated allele
721 frequencies as well as ANGSD does. In the second method (b F_{ST}), GPAT implements a
722 Bayesian framework as described by (Holsinger, Lewis, & Dey, 2002). This Bayesian
723 approach has the advantage of being able to provide a confidence interval for F_{ST} , but it is
724 computationally expensive.

725

726

727 **References for software in Table 2 of the main text**
728
729 AlphaAssign (Whalen, Gorjanc, & Hickey, 2019)
730 Angsd (Korneliussen et al., 2014)
731 Atlas (Link et al., 2017)
732 BaseVar (Liu et al., 2018)
733 Bcftools/ROH (Narasimhan et al., 2016)
734 EBG (Blischak et al., 2018)
735 Entropy (Gompert et al., 2014)
736 evalAdmix (Garcia-Erill & Albrechtsen, 2020)
737 Freebayes (Garrison & Marth, 2012)
738 GATK (McKenna et al., 2010)
739 GPAT (Domyan et al., 2016)
740 GUS-LD (Bilton et al., 2018)
741 Heterozygosity-em (Bryc, Patterson, & Reich, 2013)
742 (<https://github.com/kasia1/heterozygosity-em>)
743 HMMploidy (<https://github.com/SamueleSoraggi/HMMploidy>)
744 LB-Impute (<https://github.com/dellaporta-laboratory/LB-Impute>)
745 LepMap3 (Rastas 2017)
746 LinkImpute (Money et al., 2015)
747 loimpute (Wasik et al., 2019)
748 lostruct (Li & Ralph, 2019)
749 MAPGD (Maruki & Lynch, 2015)
750 ngsAdmix (Skotte et al., 2013)
751 ngsDist (Vieira, Lassalle, Korneliussen, & Fumagalli, 2016)
752 ngsF (Vieira, Fumagalli, Albrechtsen, & Nielsen, 2013)
753 ngsF-HMM (Vieira, Albrechtsen, & Nielsen, 2016)
754 ngsLD (Fox et al., 2019)
755 ngsRelate (Korneliussen & Moltke, 2015)
756 ngsTools (Fumagalli et al., 2014)
757 NOISYmputer (Lorieux, Gkanogiannis, Fragoso, & Rami, 2019)
758 Ohana (Cheng, Mailund, & Nielsen, 2017; Cheng et al., 2019)
759 PCAngsd (Meisner & Albrechtsen, 2018)
760 PopLD (Maruki & Lynch, 2014)
761 Reveel (Huang, Wang, Chen, Bercovici, & Batzoglou, 2016)
762 skmer (Sarmashghi, Bohmann, P Gilbert, Bafna, & Mirarab, 2019)
763 SNPTTEST (Marchini, Howie, Myers, McVean, & Donnelly, 2007)
764 STITCH (Davies et al., 2016)
765 svgem (Lucas-Lledó, Vicente-Salvador, Aguado, & Cáceres, 2014)
766 vcflib (<https://github.com/vcflib/vcflib>)
767 WHODAD (Snyder-Mackler et al., 2016)
768
769

770 **Supplementary tables**

771

772 **Table S1.** List of population genomics studies using lcWGS.

773

Cayuela, Hugo, Clément Rougeux, Martin Laporte, Claire Mérot, Eric Normandeau, Maëva Leitwein, Yann Dorant, et al. 2021. "Genome-Wide DNA Methylation Predicts Environmentally-Driven Life History Variation in a Marine Fish." <i>bioRxiv</i> . https://doi.org/10.1101/2021.01.28.428603 .
Clucas, Gemma V., R. Nicolas Lou, Nina O. Therkildsen, and Adrienne I. Kovach. 2019. "Novel Signals of Adaptive Genetic Variation in Northwestern Atlantic Cod Revealed by Whole-genome Sequencing." <i>Evolutionary Applications</i> 134 (4): 1289.
Crawford, Jacob E., Ricardo Amaru, Jihyun Song, Colleen G. Julian, Fernando Racimo, Jade Yu Cheng, Xiuqing Guo, et al. 2017. "Natural Selection on Genes Related to Cardiovascular Health in High-Altitude Adapted Andeans." <i>American Journal of Human Genetics</i> 101 (5): 752–67.
Foote, Andrew D., Michael D. Martin, Marie Louis, George Pacheco, Kelly M. Robertson, Mikkel Holger S. Sinding, Ana R. Amaral, et al. 2019. "Killer Whale Genomes Reveal a Complex History of Recurrent Admixture and Vicariance." <i>Molecular Ecology</i> 8 (7): e1002837–18.
Foote, Andrew D., Nagarjun Vijay, María C. Ávila-Arcos, Robin W. Baird, John W. Durban, Matteo Fumagalli, Richard A. Gibbs, et al. 2016. "Genome-Culture Coevolution Promotes Rapid Divergence of Killer Whale Ecotypes." <i>Nature Communications</i> 7 (January): 11693.
Fuller, Zachary L., Veronique J. L. Mocellin, Luke A. Morris, Neal Cantin, Jihanne Shepherd, Luke Sarre, Julie Peng, et al. 2020. "Population Genetics of the Coral <i>Acropora Millepora</i> : Toward Genomic Prediction of Bleaching." <i>Science</i> 369 (6501). https://doi.org/10.1126/science.aba4674 .
Gignoux-Wolfsohn, Sarah A., Malin L. Pinsky, Kathleen Kerwin, Carl Herzog, Mackenzie Hall, Alyssa B. Bennett, Nina H. Fefferman, and Brooke Maslo. 2021. "Genomic Signatures of Selection in Bats Surviving White-Nose Syndrome." <i>Molecular Ecology</i> . https://onlinelibrary.wiley.com/doi/abs/10.1111/mec.15813?casa_token=erFTF_VQsOkAAAAA:eptQO8l66AX6xJVdRd6iv90BA9avfwJVDnQyG9sb_IWAd0aoJNYK6mI7P_qFrAMo-fBbCKAOD2DWrg .
Ilardo, Melissa A., Ida Moltke, Thorfinn S. Korneliussen, Jade Cheng, Aaron J. Stern, Fernando Racimo, Peter de Barros Damgaard, et al. 2018. "Physiological and Genetic Adaptations to Diving in Sea Nomads." <i>Cell</i> 173 (3): 569–80.e15.
Jones, Felicity C., Manfred G. Grabherr, Yingguang Frank Chan, Pamela Russell, Evan Mauceli, Jeremy Johnson, Ross Swofford, et al. 2012. "The Genomic Basis of Adaptive Evolution in Threespine Sticklebacks." <i>Nature</i> 484 (7392): 55–61.
Liu, Shiping, Eline D. Lorenzen, Matteo Fumagalli, Bo Li, Kelley Harris, Zijun Xiong, Long Zhou, et al. 2014. "Population Genomics Reveal Recent Speciation and Rapid Evolutionary Adaptation in Polar Bears." <i>Cell</i> 157 (4): 785–94.
Mérot, Claire, Emma Berdan, Hugo Cayuela, Haig Djambazian, Anne-Laure Ferchaud, Martin Laporte, Eric Normandeau, Jiannis Ragoussis, Maren Wellenreuther, and Louis Bernatchez. 2021. "Locally-Adaptive Inversions Modulate Genetic Variation at Different Geographic Scales in a Seaweed Fly." <i>bioRxiv</i> . https://doi.org/10.1101/2020.12.28.424584 .
Oziolor, Elias M., Noah M. Reid, Sivan Yair, Kristin M. Lee, Sarah Guberman VerPloeg, Peter C. Bruns, Joseph R. Shaw, Andrew Whitehead, and Cole W. Matson. 2019. "Adaptive Introgression Enables Evolutionary Rescue from Extreme Environmental Pollution." <i>Science</i> 364 (6439): 455–57.
Powell, Daniel L., Mateo García-Olazábal, Mackenzie Keegan, Patrick Reilly, Kang Du, Alejandra P. Díaz-Loyo, Shreya Banerjee, et al. 2020. "Natural Hybridization Reveals Incompatible Alleles That Cause Melanoma in Swordtail Fish." <i>Science</i> 368 (6492): 731–36.
Reid, Noah M., Dina A. Proestou, Bryan W. Clark, Wesley C. Warren, John K. Colbourne, Joseph R.

Shaw, Sibel I. Karchner, et al. 2016. "The Genomic Landscape of Rapid Repeated Evolutionary Adaptation to Toxic Pollution in Wild Fish." *Science* 354 (6317): 1305–8.

Rowan, Beth A., Darren Heavens, Tatiana R. Feuerborn, Andrew J. Tock, Ian R. Henderson, and Detlef Weigel. 2019. "An Ultra High-Density Arabidopsis Thaliana Crossover Map That Refines the Influences of Structural Variation and Epigenetic Features." *Genetics* 213 (3): 771–87.

Szarmach, Stephanie J., Alan Brelford, Christopher Witt, and David P. L. Toews. 2021. "Comparing Divergence Landscapes from Reduced-Representation and Whole-Genome Re-Sequencing in the Yellow-Rumped Warbler (*Setophaga Coronata*) Species Complex." *bioRxiv*.
<https://doi.org/10.1101/2021.03.23.436663>.

Therkildsen, Nina O., Aryn P. Wilder, David O. Conover, Stephan B. Munch, Hannes Baumann, and Stephen R. Palumbi. 2019. "Contrasting Genomic Shifts Underlie Parallel Phenotypic Evolution in Response to Fishing." *Science* 365 (6452): 487–90.

Wang, Hongru, Filipe G. Vieira, Jacob E. Crawford, Chengcai Chu, and Rasmus Nielsen. 2017. "Asian Wild Rice Is a Hybrid Swarm with Extensive Gene Flow and Feralization from Domesticated Rice." *Genome Research* 27 (6): 1029–38.

Wilder, Aryn P., Stephen R. Palumbi, David O. Conover, and Nina Overgaard Therkildsen. 2020. "Footprints of Local Adaptation Span Hundreds of Linked Genes in the Atlantic Silverside Genome." *Evolution Letters* 4 (5): 430–43.

775
776
777

Table S2. Model parameters used for forward genetic simulation.

Scenario*	Chromosome length (in Mb)	Number of populations	Population size (N) [†]	Mutation rate (μ)	Recombination rate (r)	Migration rate (m)	Selection coefficient (s)	Corresponding figures
Single population	30	1	1000	10^{-6}	2.5×10^{-6}	NA	NA	3-4, S1-7
Spatial structure (low migration)	30	9	500	2×10^{-7}	5×10^{-7}	0.0005	NA	5A, S10
Spatial structure (high migration)	30	9	500	2×10^{-7}	5×10^{-7}	0.002	NA	5B, S11
Spatial structure (high migration, longer chromosome)	300	9	500	2×10^{-7}	5×10^{-7}	0.002	NA	S9
Divergent selection[‡] (large N_e, high migration)	30	2	5000	10^{-7}	2.5×10^{-7}	0.001	0.08	6-7
Divergent selection[‡] (small N_e, low migration)	30	2	5000	2×10^{-8}	5×10^{-8}	0.0005	0.08	S12-14
Imputation test (low diversity, high LD)	30	1	1000	10^{-8}	5×10^{-9}	NA	NA	9, S16-20
Imputation test (medium diversity, medium LD)	30	1	1000	10^{-7}	5×10^{-8}	NA	NA	9, S16-20
Imputation test (medium diversity, low LD)	30	1	1000	10^{-7}	2.5×10^{-7}	NA	NA	9, S16-20

778
779
780
781
782
783
784
785
786

* Each entry is linked to its corresponding simulation pipeline on GitHub.

[†] Note that since we scaled down population size and scaled up mutation rate, recombination rate, migration rate, and selection coefficient in order to speed up computation, these population sizes do not represent the effective population size of our simulated populations.

[‡] These parameters are the ones used in the selection stage of the simulation. Prior to the selection stage, a burn-in stage was first performed, during which the population size was further scaled down, whereas mutation rate and recombination rate were scaled up, all by a factor of 10. See supplementary methods for details.

787
788
789
790

Table S3. *Heliconius erato* short read archive (SRA) IDs. Individuals used for the subsampling and genotype-likelihood-based analysis of *H. erato* subspecies, with SRA ID and subspecies names. Samples from (Van Belleghem et al., 2017).

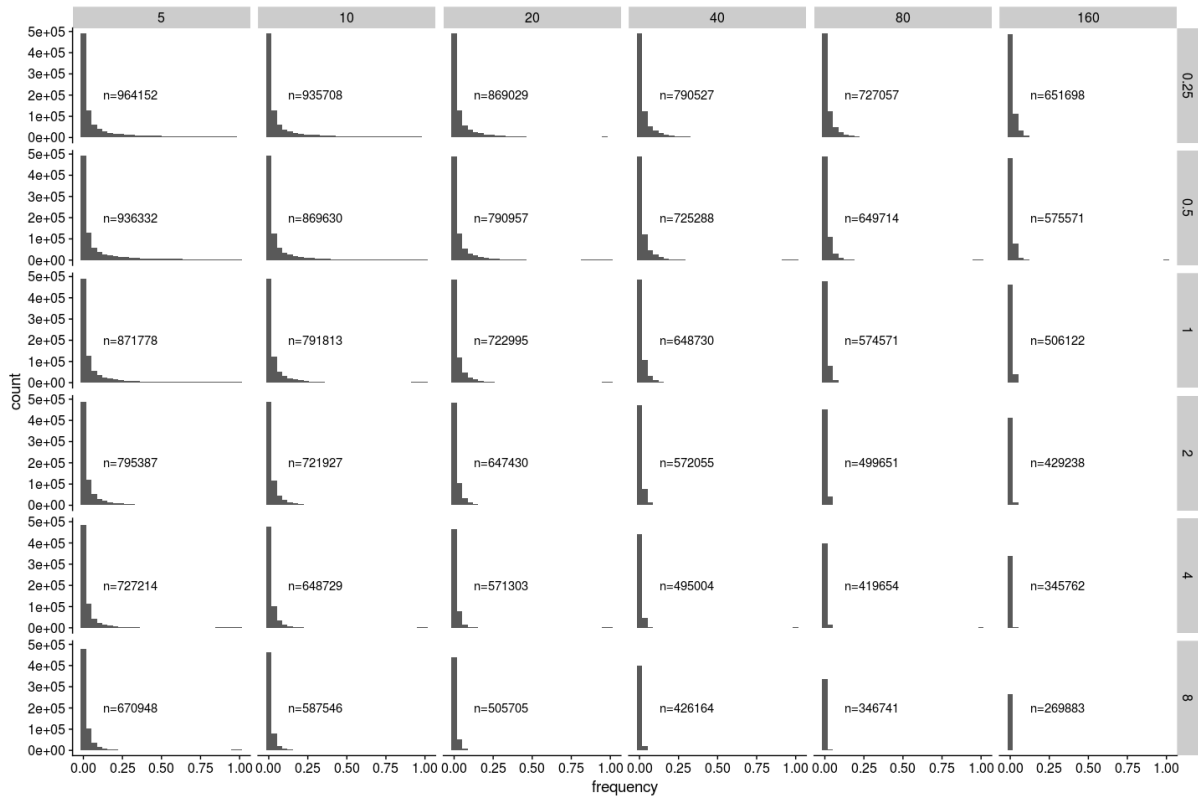
SRA ID	<i>H. erato</i> subspecies
SRS1618075	amalfreda
SRS1618086	amalfreda
SRS1618008	amalfreda
SRS1618009	amalfreda
SRS1618010	amalfreda
SRS1618033	emma
SRS1618034	emma
SRS1618062	emma
SRS1618063	emma
SRS1618065	emma
SRS1618066	emma
SRS1618067	emma
SRS1618069	erato
SRS1618070	erato
SRS1618071	erato
SRS1618072	erato
SRS1618073	erato
SRS1618084	erato
SRS1618014	etylus
SRS1618015	etylus
SRS1618016	etylus
SRS1618017	etylus
SRS1618018	etylus
SRS1618053	lativitta
SRS1618044	lativitta
SRS1618045	lativitta
SRS1618046	lativitta
SRS1618047	lativitta
SRS1618002	demophoon

SRS1618093	demophoon
SRS1618094	demophoon
SRS1618098	demophoon
SRS1618100	demophoon
SRS1617995	demophoon
SRS1618032	favorinus
SRS1618057	favorinus
SRS1618056	favorinus
SRS1618058	favorinus
SRS1618059	favorinus
SRS1618060	favorinus
SRS1618083	favorinus
SRS1618102	hydara
SRS1617999	hydara
SRS1618068	hydara
SRS1618074	hydara
SRS1618087	hydara
SRS1618101	hydara
SRS1618005	notabilis
SRS1618012	notabilis
SRS1618090	notabilis
SRS1618091	notabilis

791
792

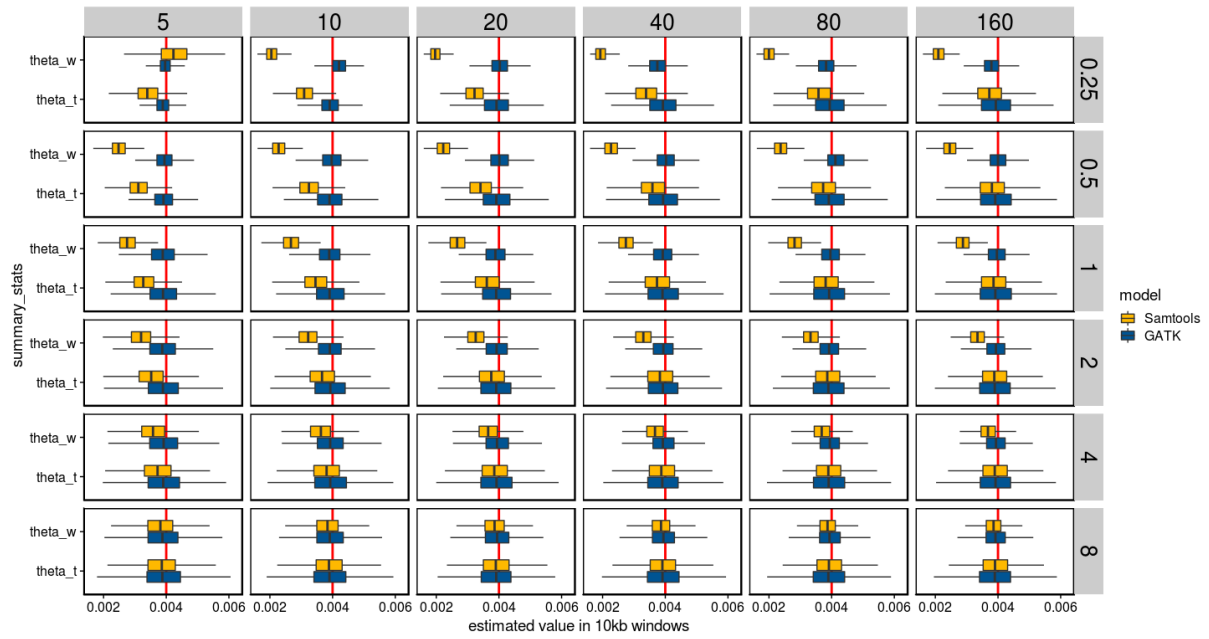
793
794
795

Supplementary figures



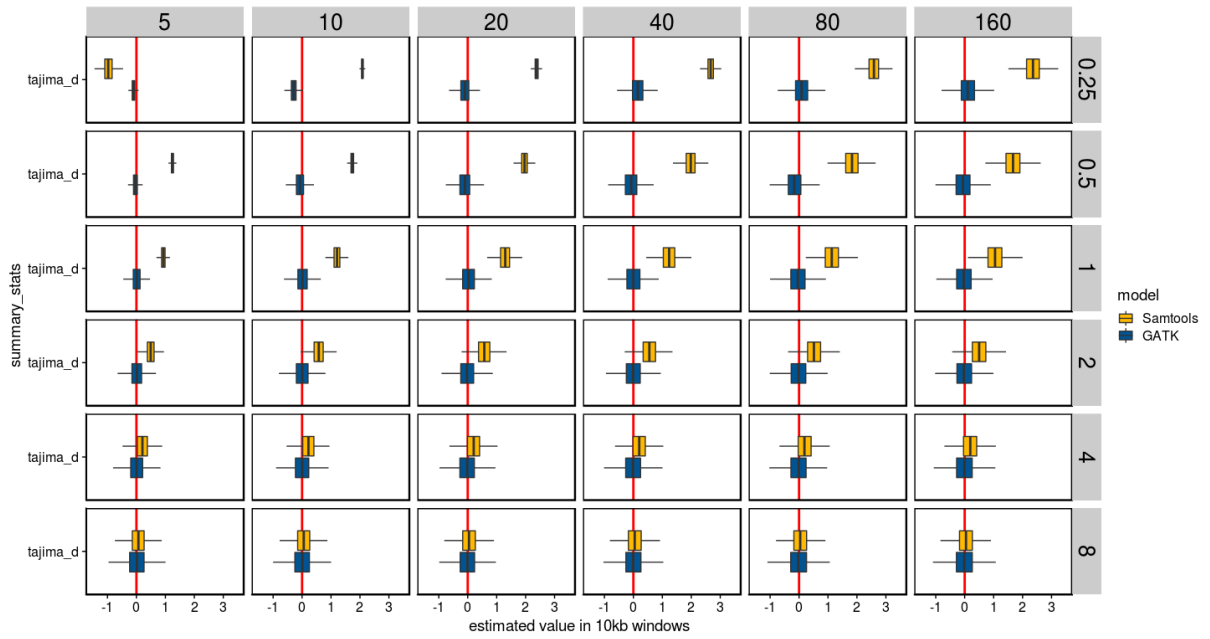
796
797
798
799
800
801

Figure S1. Histogram of the allele frequencies of false negative SNPs with IcWGS. Across the different facets, sample size increases from left to right, and coverage increases from top to bottom. The total sequencing effort remains the same along the diagonal from bottom left to top right.



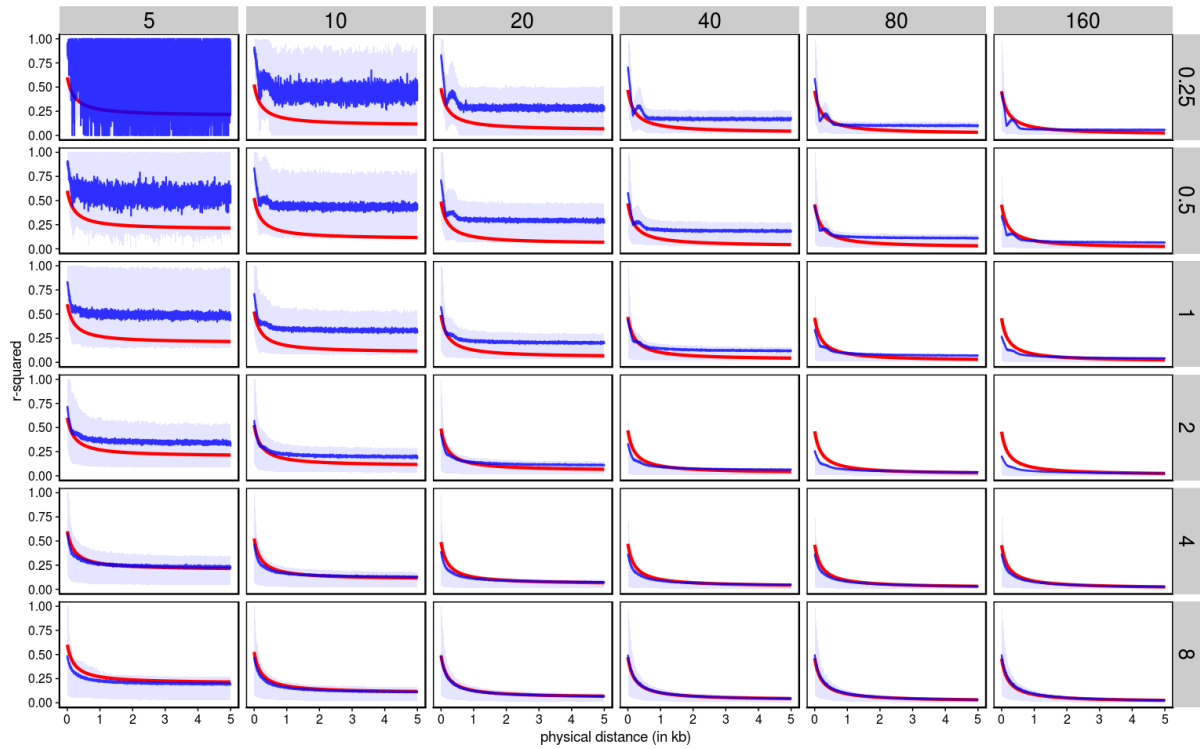
802
803
804
805
806
807
808
809

Figure S2. Distribution of Tajima's θ (aka π) and Watterson's θ estimated using the Samtools genotype likelihood model and the GATK genotype likelihood model in 10kb windows. Across the different facets, sample size increases from left to right, and coverage increases from top to bottom. The total sequencing effort remains the same along the diagonal from bottom left to top right. The true chromosome-average values for both statistics should be 0.004, which is marked with a read line.



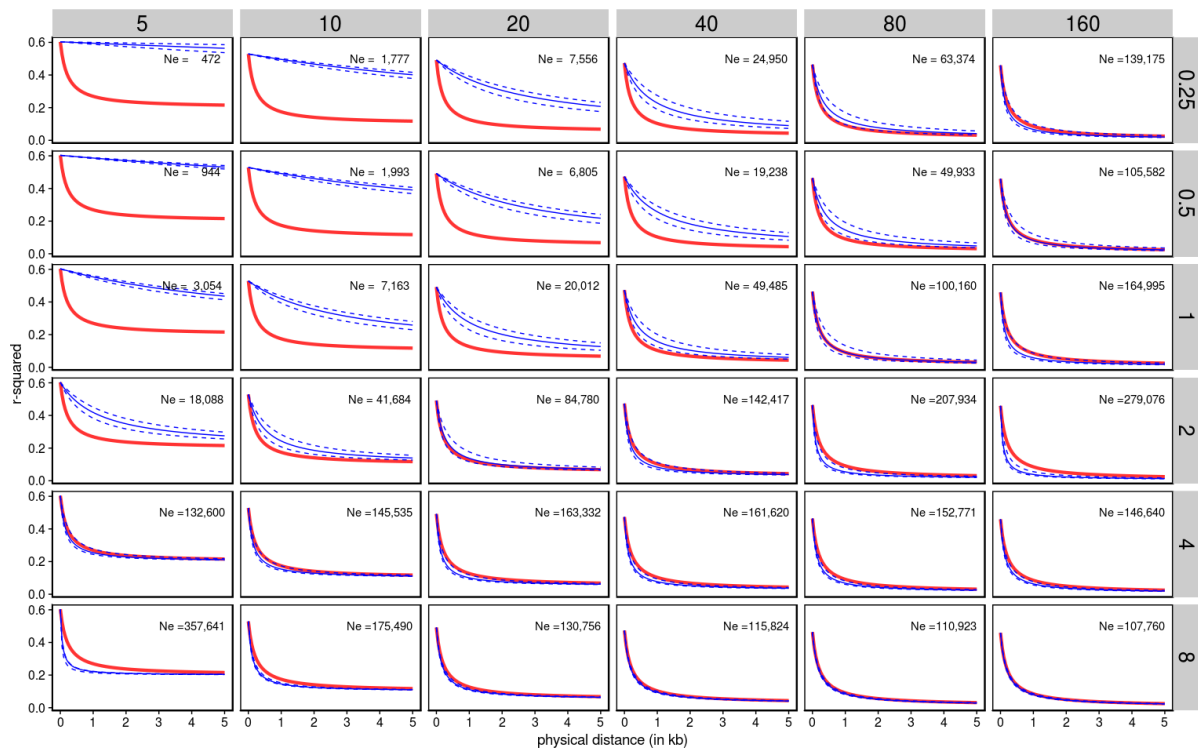
810
 811
 812
 813
 814
 815
 816
 817

Figure S3. Tajima's D estimated using the Samtools genotype likelihood model and the GATK genotype likelihood model in 10kb windows. Across the different facets, sample size increases from left to right, and coverage increases from top to bottom. The total sequencing effort remains the same along the diagonal from bottom left to top right. The true chromosome-average Tajima's D should be 0, which is marked with a red line.



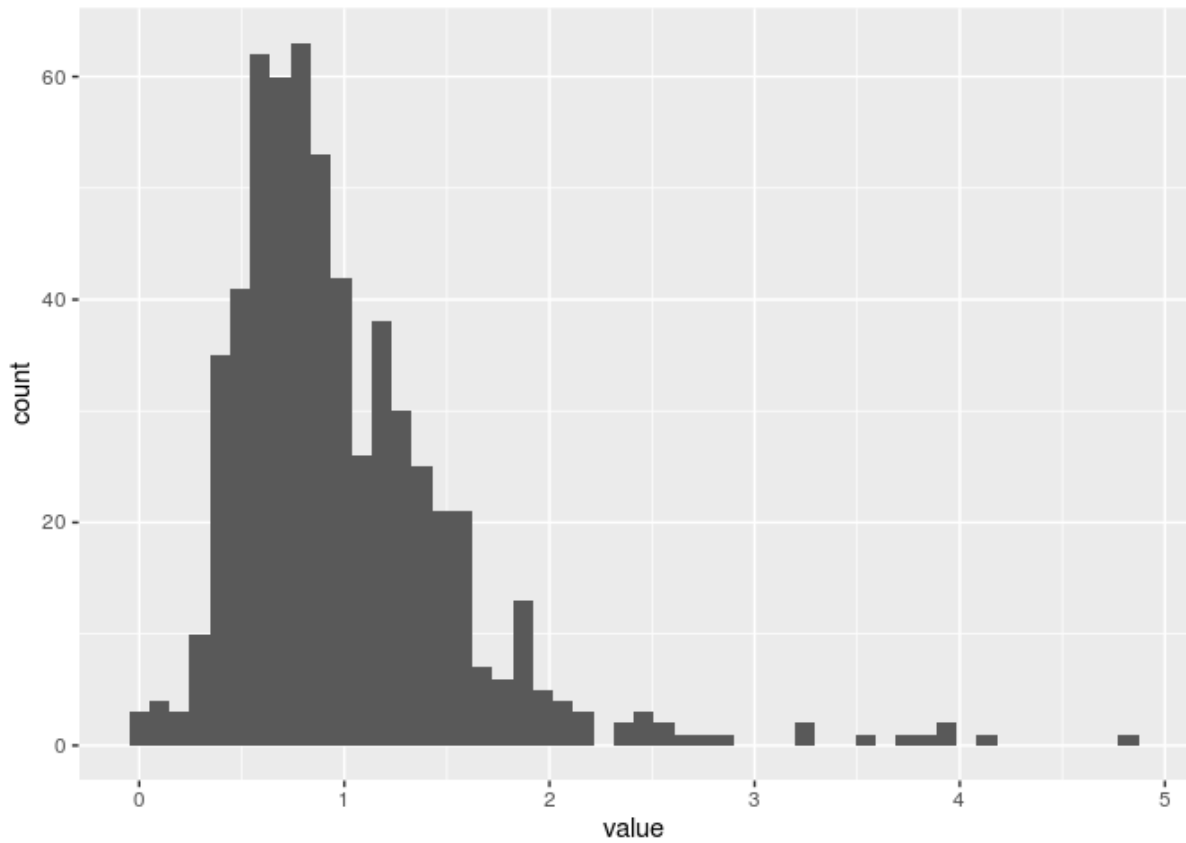
818
 819
 820
 821
 822
 823
 824
 825
 826
 827
 828

Figure S4. Linkage disequilibrium (LD) estimated using ngsLD from simulated data. LD, shown on the y axis, is measured as r^2 between pairs of SNPs, and the physical distance between these SNP pairs is shown on the x axis. The blue line shows the mean of the estimated r^2 for each distance value, and the lighter blue area shows its interquartile range. The red line marks the theoretical expectation of r^2 under mutation-drift equilibrium. Across the different facets, sample size increases from left to right, and coverage increases from top to bottom. The total sequencing effort remains the same along the diagonal from bottom left to top right.

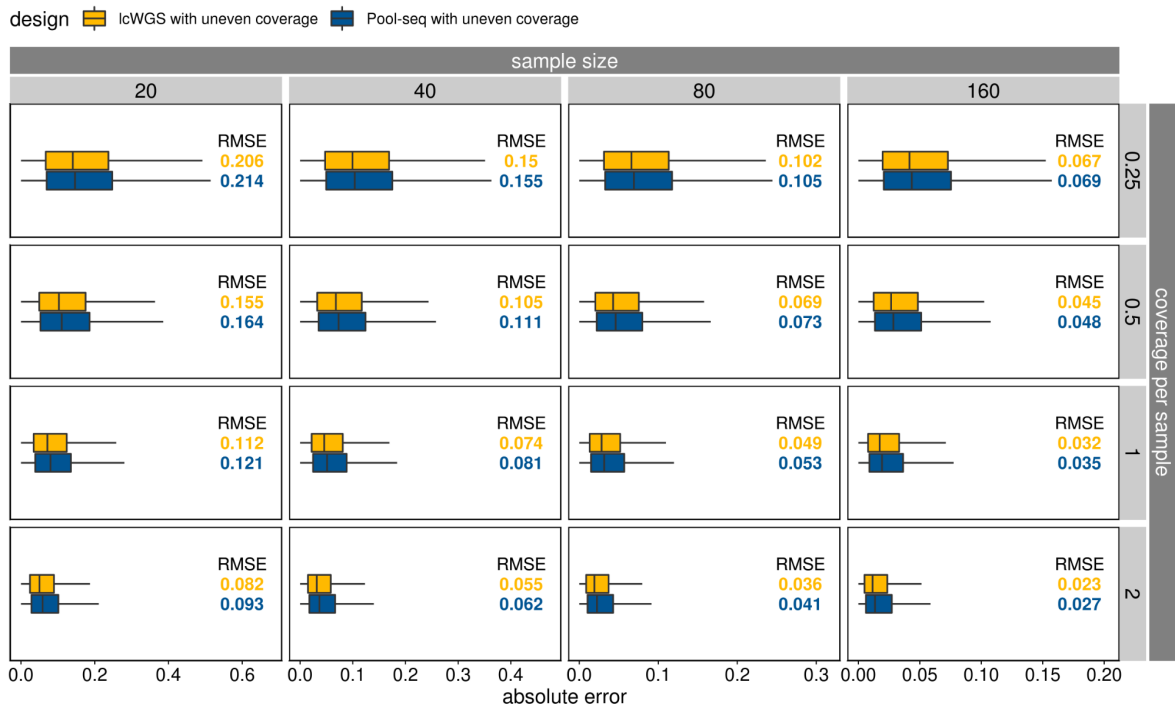


829
830
831
832
833
834
835
836
837
838
839
840
841

Figure S5. Estimated linkage disequilibrium (LD) fitted to a linkage decay model using ngsLD. The solid blue line shows the best fitted model, and the dashed blue lines represent its 95% confidence interval. When the true recombination rate is known, the effective population size (N_e) can be calculated from the estimated LD decay rate and is shown on the top right corner in each facet. The true effective population size used in the simulation is 100,000. The red line marks the theoretical expectation of r^2 under mutation-drift equilibrium, given by (Hill & Weir, 1988). Across the different facets, sample size increases from left to right, and coverage increases from top to bottom. The total sequencing effort remains the same along the diagonal from bottom left to top right.



842
 843 **Figure S6.** The sequencing coverage distribution that we sampled from when simulating
 844 uneven sequencing coverage among samples. This distribution is obtained by merging the
 845 distributions of coverage among samples from three of our lcWGS projects where we pooled
 846 samples by molarity.



847

848

849

850

851

852

853

854

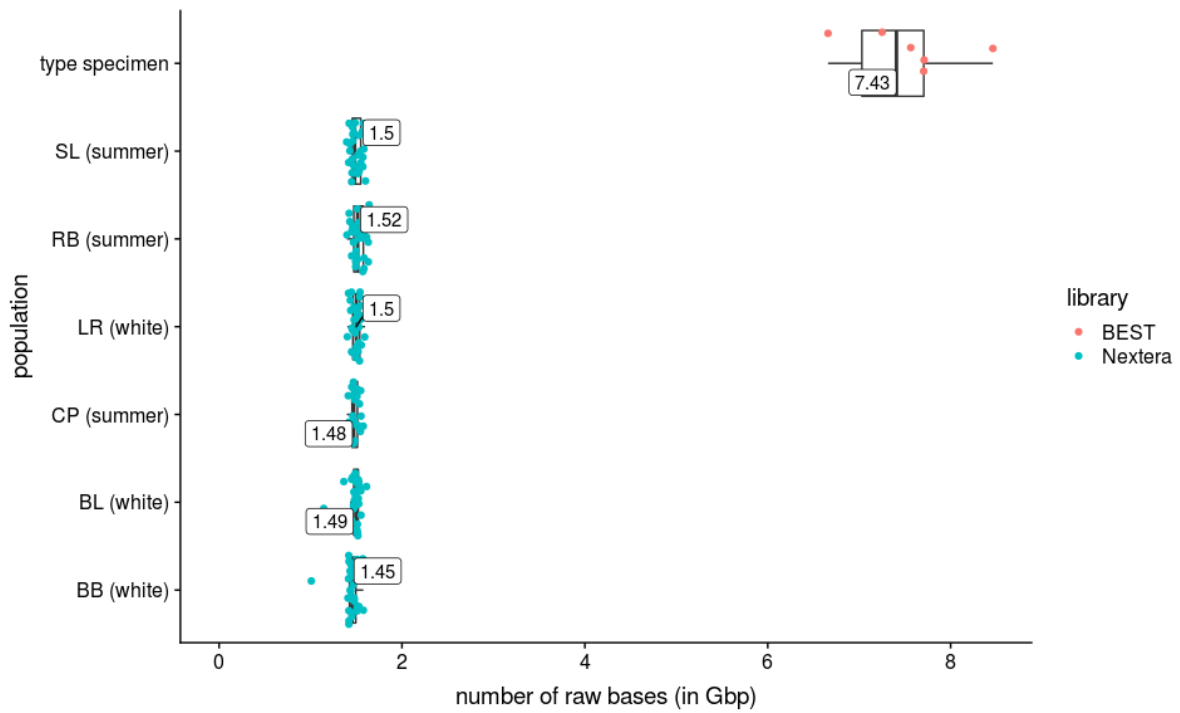
855

856

857

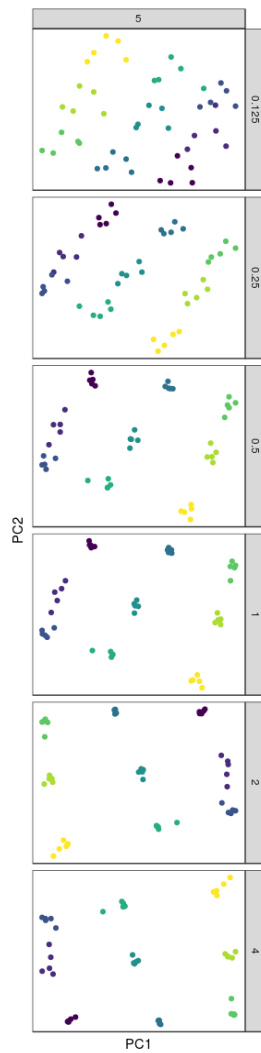
858

Figure S7. The error in allele frequency estimation with lcWGS (yellow) and Pool-seq (blue) data, both with uneven coverage among individual samples. The distribution of absolute errors ($|\text{estimated frequency} - \text{true frequency}|$) is shown with the box plots along the x-axis. The lower and upper hinges of the box plots show 25th and 75th percentile of the absolute errors, and the whiskers extend to the largest or smallest values no further than 1.5 times the interquartile range. Outlier points are hidden. Across the different facets, sample size increases from left to right, and coverage increases from top to bottom. The total sequencing effort remains the same along the diagonal from bottom left to top right. The root mean squared error (RMSE) for the two sequencing designs are shown in each facet. False negative SNPs are not included in this figure. See supplementary methods and Figure S7 for how uneven coverage was simulated.



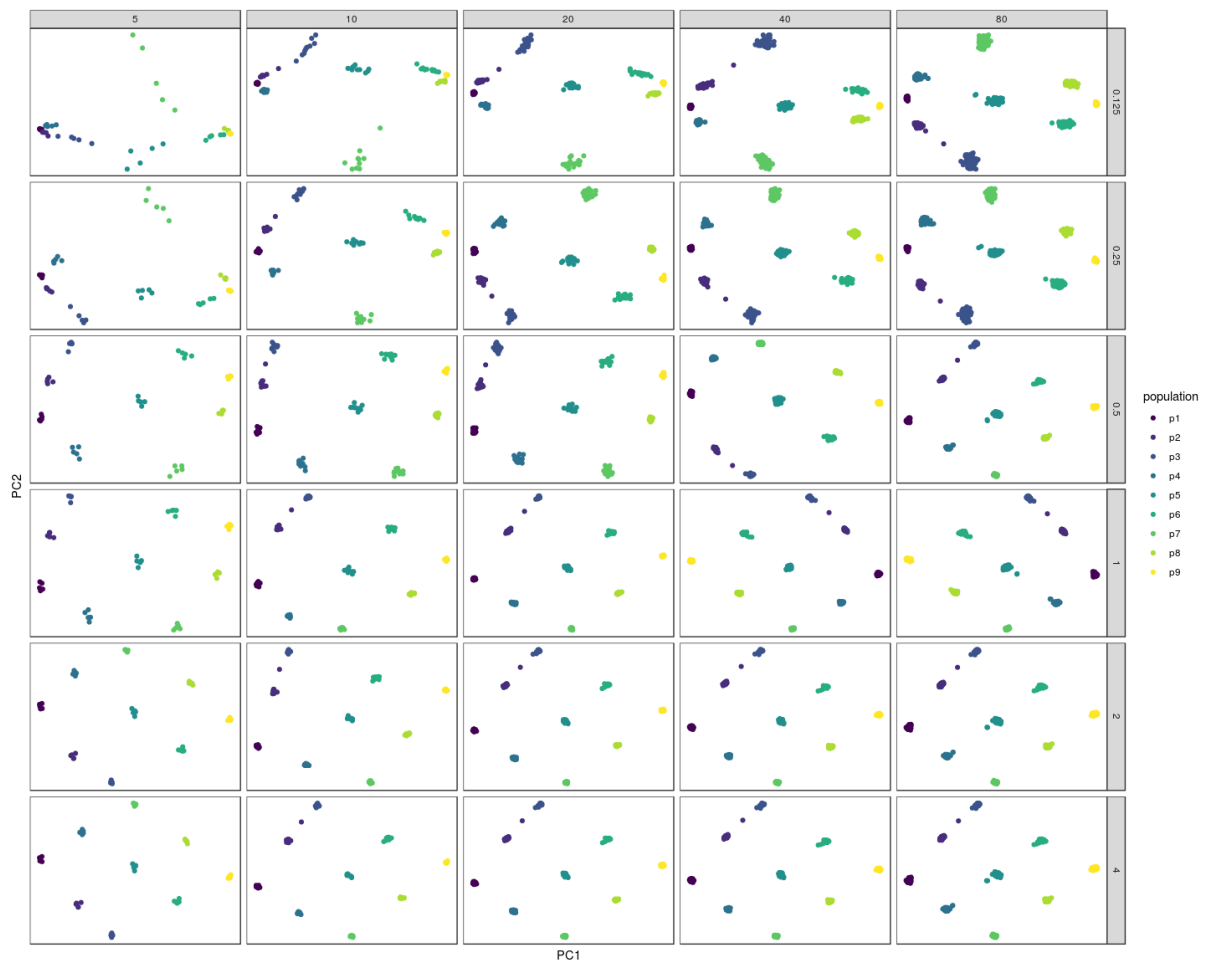
859
 860
 861
 862
 863
 864
 865
 866
 867
 868
 869
 870
 871
 872
 873
 874

Figure S8. An empirical example from one of our lcWGS projects of the distribution of raw sequencing yield from individual samples when they are resequenced based on the first round of sequencing. This is to demonstrate that equal distribution of sequencing effort can be approximated by such a sequencing design. (The type specimens were designed to have higher sequencing yield than other samples.)



875
 876
 877
 878
 879
 880
 881
 882
 883
 884
 885
 886

Figure S9. The spatial population structures inferred through principal component analysis (PCA) with lcWGS data using PCA. The first two principal components are shown. This result is from our higher gene flow scenario (an average of 1 effective migrant from one population to another every generation), but a longer chromosome is simulated (300Mbp, or 10 times longer than the scenarios shown in Figure 4). Sample size remains five per sample, and coverage increases from top to bottom.



888

889

890

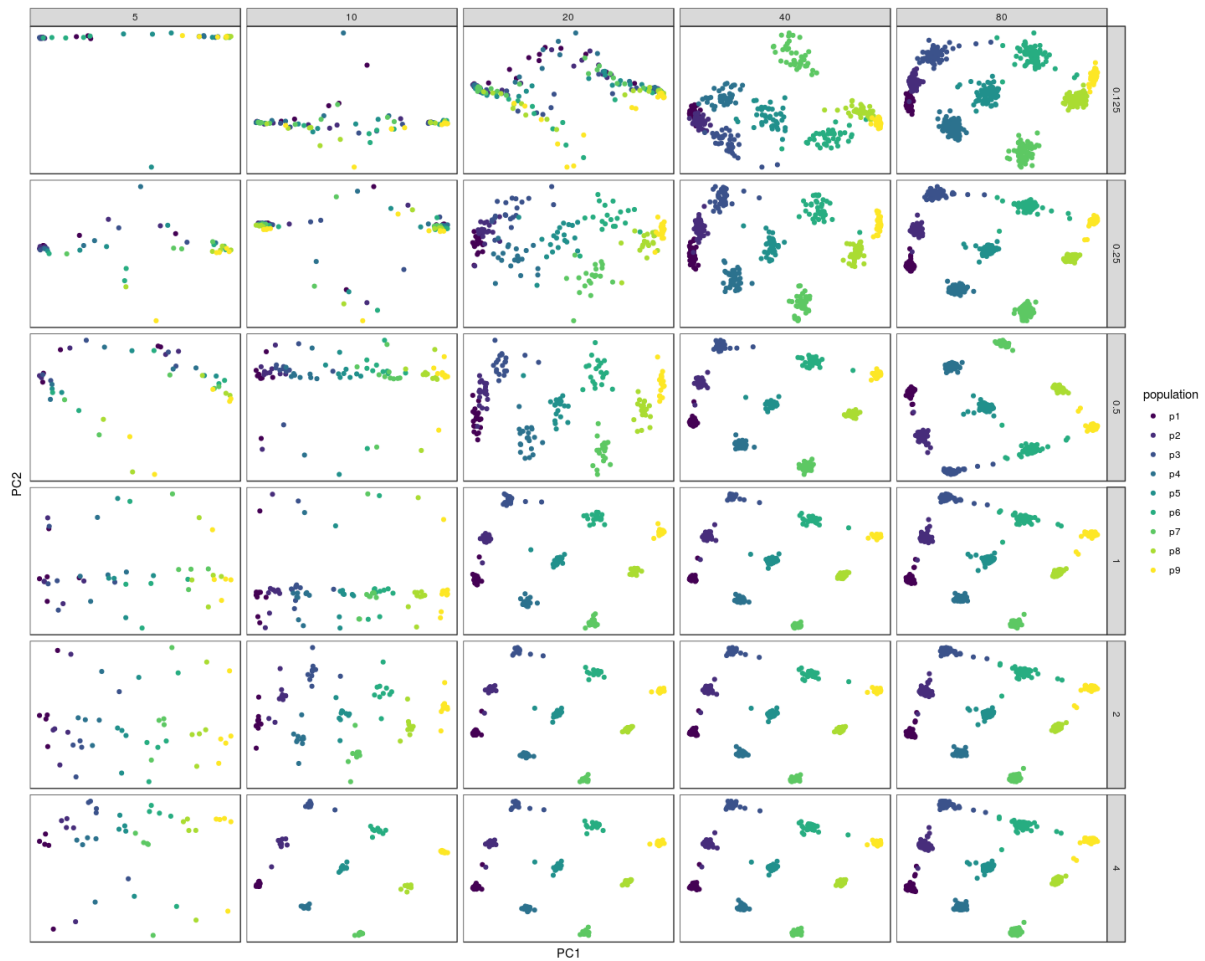
891

892

893

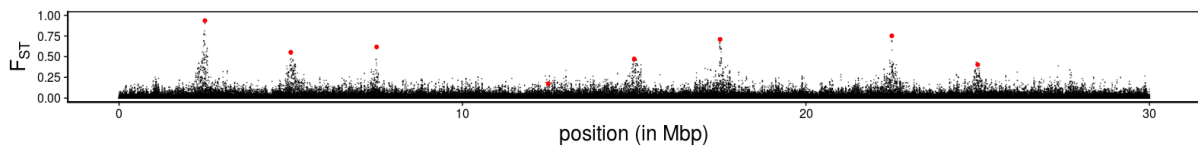
894

Figure S10. Patterns of spatial population structure inferred through principal component analysis (PCA) with lcWGS data using PCAngsd, in a scenario with lower gene flow (an average of 0.25 effective migrants per generation). Sample size per population increases across panels from left to right, and coverage per sample increases from top to bottom. This figure is based on the same dataset as Figure 5A, in which case ANGSD was used instead of PCAngsd to perform the PCA.



895
 896 **Figure S11.** Patterns of spatial population structure inferred through principal component
 897 analysis (PCA) with lcWGS data using PCAngsd, in a scenario with higher gene flow (an
 898 average of 1 effective migrants per generation). Sample size per population increases
 899 across panels from left to right, and coverage per sample increases from top to bottom. This
 900 figure is based on the same dataset as Figure 5B, in which case ANGSD was used instead
 901 of PCAngsd to perform the PCA.

902



903

904

905

906

907

908

909

910

911

912

913

914

915

916

917

918

919

920

921

922

923

924

925

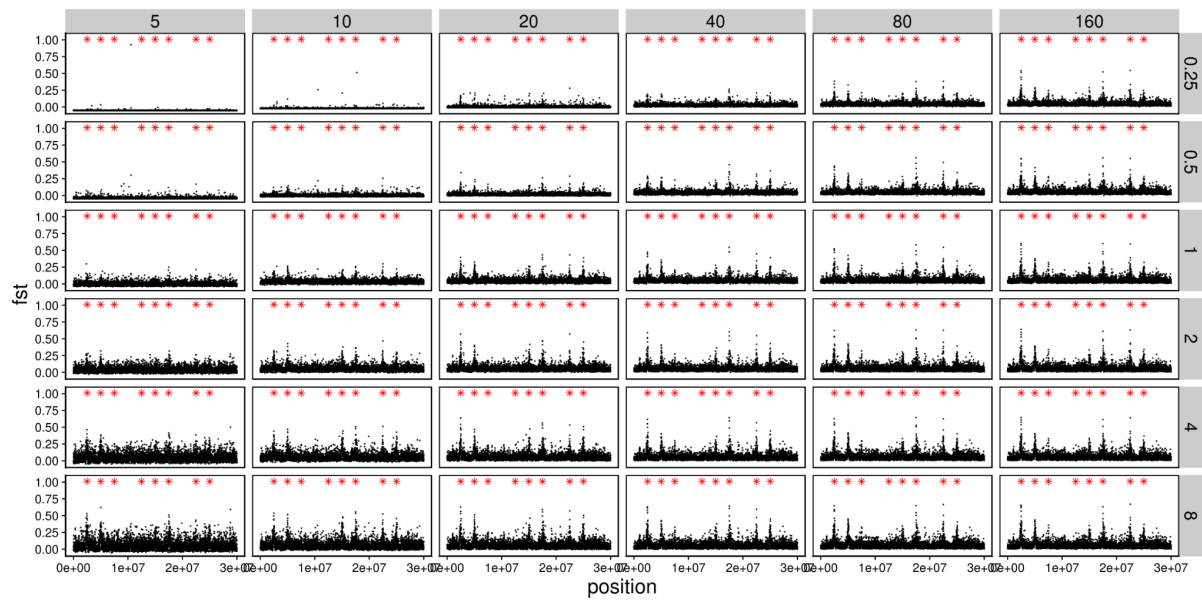
926

927

928

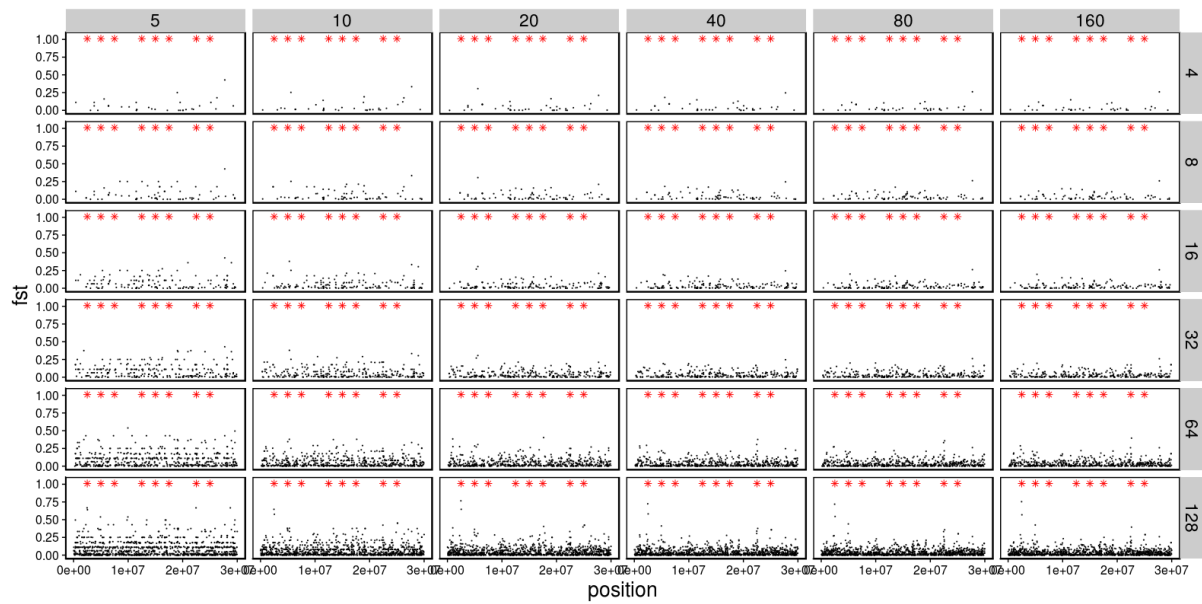
929

Figure S12. The true per-SNP F_{ST} values along the chromosome between the two simulated populations in a scenario with smaller N_e ($N_e = 10^4$) and lower gene flow (an average of 2.5 effective migrants from one population to the other every generation). Neutral SNPs are shown in black and selected SNPs are shown in black.



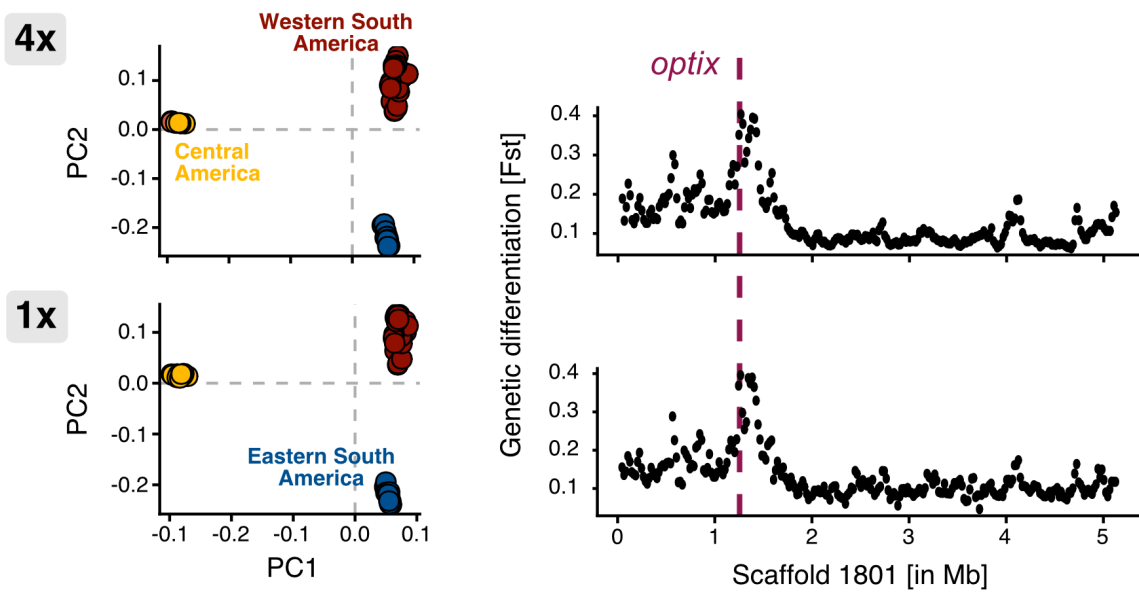
930
 931 **Figure S13.** Genome-wide scan for divergent selection with lcWGS data in a scenario with
 932 smaller N_e ($N_e = 10^4$) and lower gene flow (an average of 2.5 effective migrants from one
 933 population to the other every generation). The F_{ST} values inferred from lcWGS data in 5kb
 934 windows along the chromosome are shown on the y axis. Sample size increases from left to
 935 right, and coverage increases from top to bottom. The black points mark both the selected
 936 and neutral SNPs, and the red asterisks only mark the positions of the selected SNPs (not
 937 their inferred F_{ST} values).

938
 939
 940
 941
 942
 943
 944
 945
 946

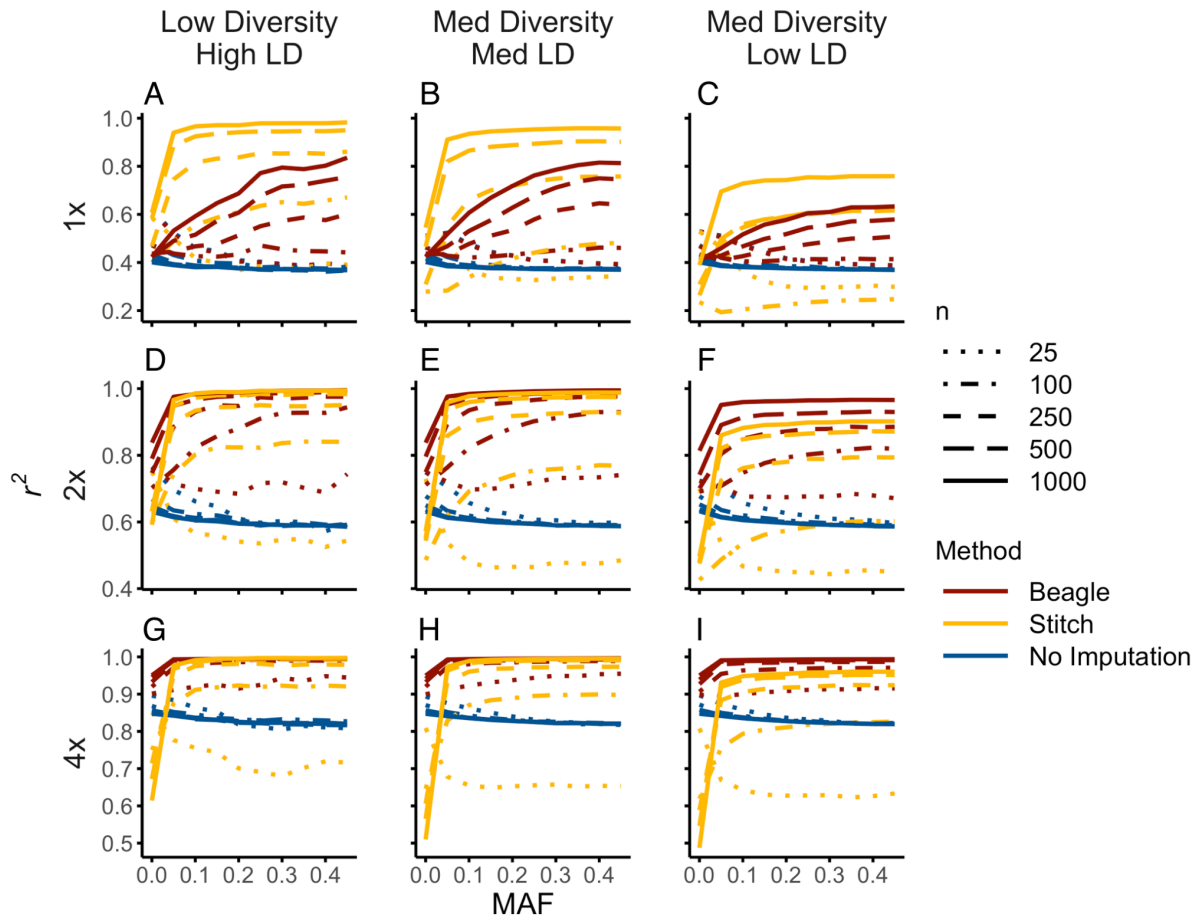


947
 948
 949
 950
 951
 952
 953
 954
 955
 956
 957

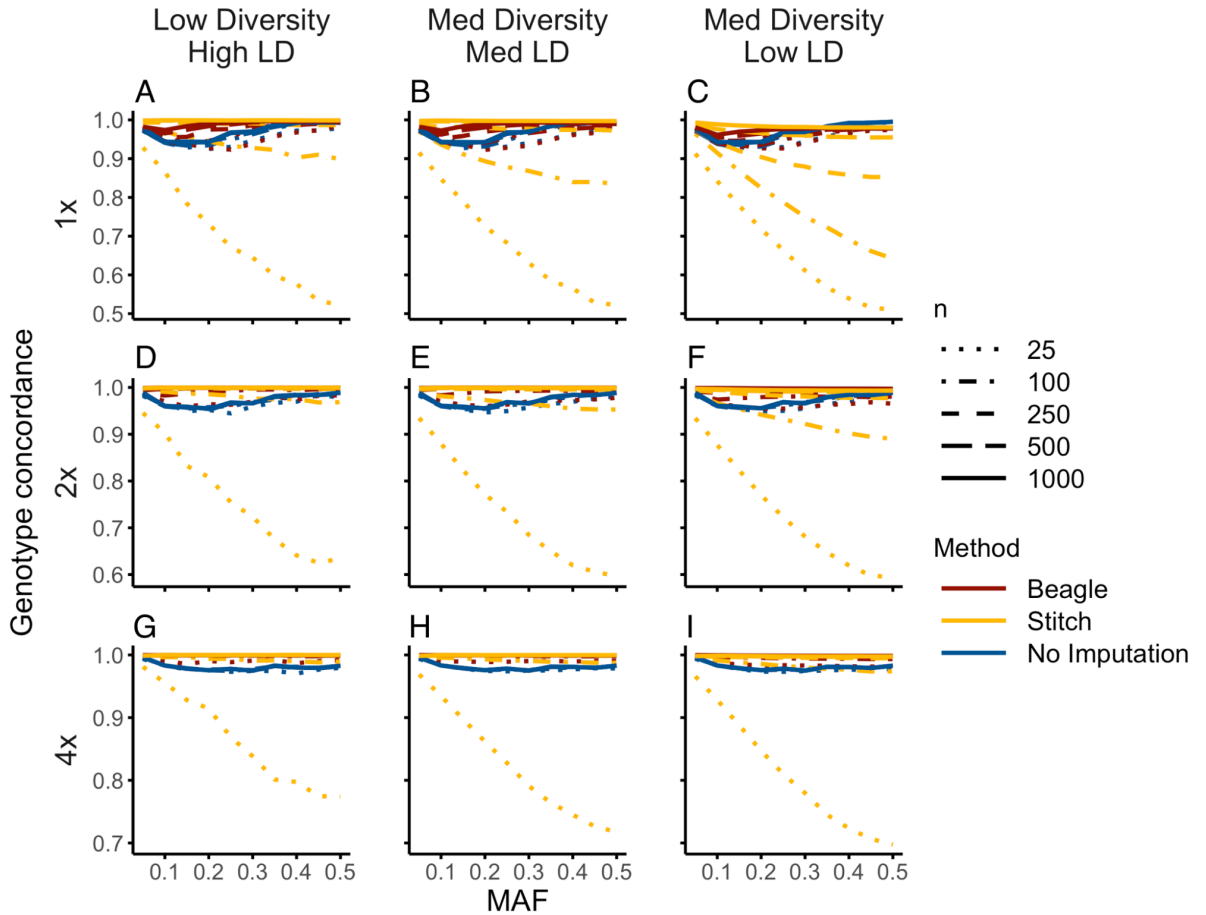
Figure S14. Genome-wide scan for divergent selection with RADseq data in a scenario with smaller N_e ($N_e = 10^4$) and lower gene flow (an average of 2.5 effective migrants from one population to the other every generation). The per-SNP F_{ST} values inferred from RAD-seq data are shown on the y axis and the SNP positions are shown on the x axis. Sample size increases from left to right, and RAD-tag density increases from top to bottom. The black points mark both the selected and neutral SNPs, and the red asterisks only mark the positions of the selected SNPs (not their inferred F_{ST} values).



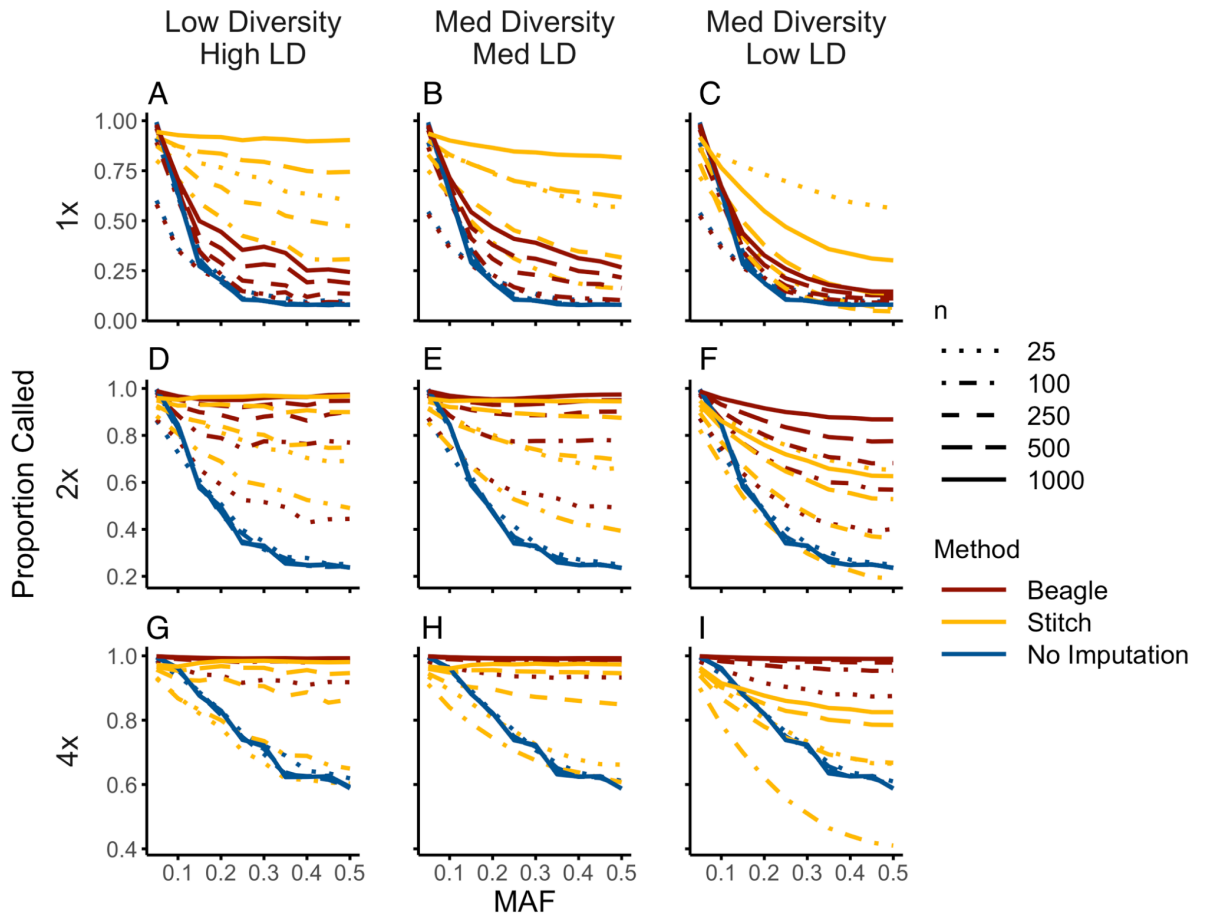
958
 959 **Figure S15.** Principal components plot and estimates of genetic differentiation around the
 960 *optix* gene for the *Heliconius* dataset at 4x (top) and 1x coverage (bottom), respectively.



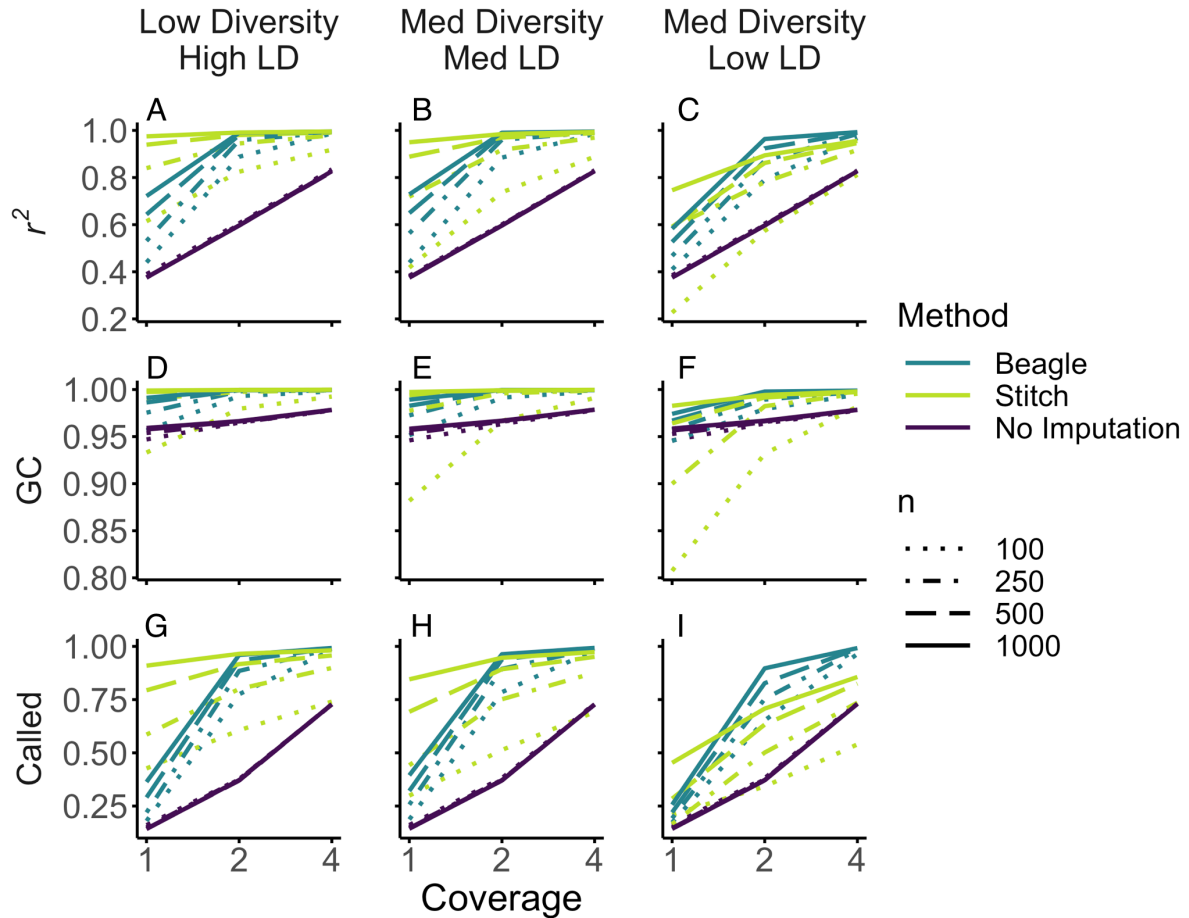
961
 962 **Figure S16.** Genotype estimation accuracy (r^2) by minor allele frequency (MAF) for
 963 imputation in STITCH and Beagle compared to posterior genotypes estimated without
 964 imputation. Combinations of sample size (n; with increasing n indicated by more contiguous
 965 lines) and sequencing coverage (plots in rows correspond to 1x, 2x and 4x coverage) were
 966 tested for each method (line colors) under different diversity and linkage disequilibrium
 967 scenarios. Note the different y-axis scales.
 968



969
 970 **Figure S17.** Genotype concordance by minor allele frequency (MAF) for imputation in
 971 STITCH and Beagle and without imputation. Genotypes were called with minimum posterior
 972 genotype probability of 0.9. Combinations of sample size (n; with increasing n indicated by
 973 more contiguous lines) and sequencing coverage (plots in rows correspond to 1x, 2x and 4x
 974 coverage) were tested for each method (line colors) under different diversity and linkage
 975 disequilibrium scenarios. Note the different y-axis scales.
 976
 977

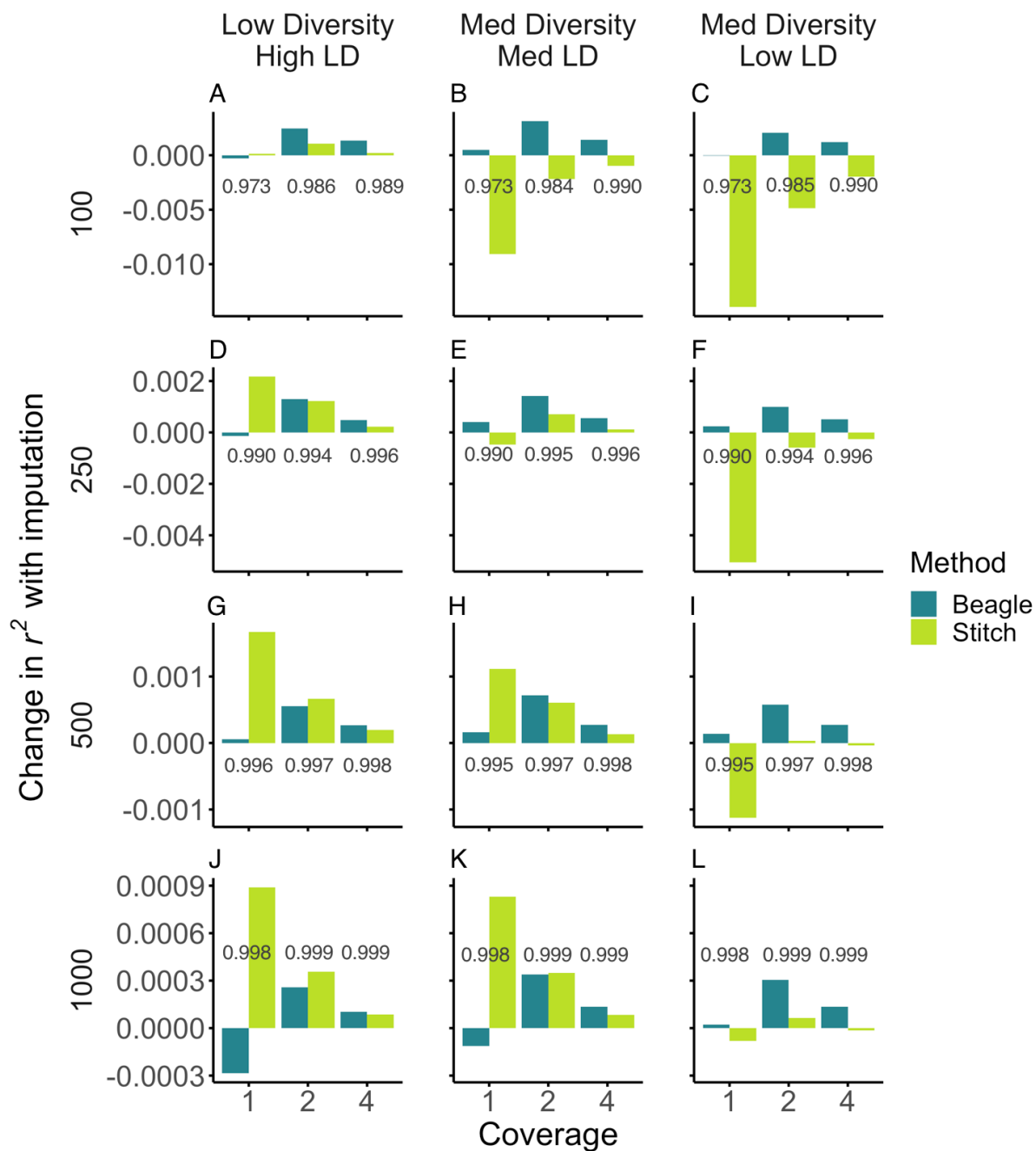


978
 979 **Figure S18.** Proportion of genotypes called by minor allele frequency (MAF) for imputation
 980 in STITCH and Beagle and without imputation. Genotypes were called with minimum
 981 posterior genotype probability of 0.9. Combinations of sample size (n; with increasing n
 982 indicated by more contiguous lines) and sequencing coverage (plots in rows correspond to
 983 1x, 2x and 4x coverage) were tested for each method (line colors) under different diversity
 984 and linkage disequilibrium scenarios. Note the different y-axis scales.



985
 986
 987
 988
 989
 990
 991
 992
 993

Figure S19. Genotype estimation by imputation in STITCH and Beagle compared to posterior genotypes estimated without imputation for sites with $MAF > 0.05$. Combinations of sample size (n ; with increasing n indicated by more contiguous lines) and sequencing coverage (x -axis) were tested for each method (line colors) under different diversity and linkage disequilibrium scenarios. **(A)-(C)** Mean r^2 between true genotypes and estimated genotype dosage. **(D)-(F)** Genotype concordance (GC) between true and called genotypes with posterior genotype probability > 0.9 . **G-I)** Proportion of genotypes called with posterior genotype probability > 0.9 .



995
 996
 997
 998
 999
 1000
 1001
 1002

Figure S20. Change in accuracy (r^2) of minor allele frequencies (MAF) estimation using imputed genotype probabilities from STITCH and Beagle, relative to non-imputed genotype likelihoods. Values above the x-axis show r^2 for MAF estimated without imputation. The three diversity/LD scenarios are arranged in columns, sample sizes ($n=100, 250, 500$ and 1000) are arranged in rows, and sequencing depths are shown on the x-axis. Note the different y-axis scales.

1003 **Supplementary References**

1004

- 1005 Allio, R., Donega, S., Galtier, N., & Nabholz, B. (2017). Large Variation in the Ratio of
 1006 Mitochondrial to Nuclear Mutation Rate across Animals: Implications for Genetic
 1007 Diversity and the Use of Mitochondrial DNA as a Molecular Marker. *Molecular Biology
 1008 and Evolution*, 34(11), 2762–2772.
- 1009 Bilton, T. P., McEwan, J. C., Clarke, S. M., Brauning, R., van Stijn, T. C., Rowe, S. J., &
 1010 Dodds, K. G. (2018). Linkage Disequilibrium Estimation in Low Coverage High-
 1011 Throughput Sequencing Data. *Genetics*, 209(2), 389–400.
- 1012 Blischak, P. D., Kubatko, L. S., & Wolfe, A. D. (2018). SNP genotyping and parameter
 1013 estimation in polyploids using low-coverage sequencing data. *Bioinformatics*, 34(3),
 1014 407–415.
- 1015 Bryc, K., Patterson, N., & Reich, D. (2013). A novel approach to estimating heterozygosity
 1016 from low-coverage genome sequence. *Genetics*, 195(2), 553–561.
- 1017 Cheng, J. Y., Mailund, T., & Nielsen, R. (2017). Fast admixture analysis and population tree
 1018 estimation for SNP and NGS data. *Bioinformatics*, 33(14), 2148–2155.
- 1019 Cheng, J. Y., Racimo, F., & Nielsen, R. (2019). Ohana: detecting selection in multiple
 1020 populations by modelling ancestral admixture components. doi: 10.1101/546408
- 1021 Davies, R. W., Flint, J., Myers, S., & Mott, R. (2016). Rapid genotype imputation from
 1022 sequence without reference panels. *Nature Genetics*, 48(8), 965–969.
- 1023 Domyan, E. T., Kronenberg, Z., Infante, C. R., Vickrey, A. I., Stringham, S. A., Bruders,
 1024 R., ... Shapiro, M. D. (2016). Molecular shifts in limb identity underlie development of
 1025 feathered feet in two domestic avian species. *eLife*, 5, e12115.
- 1026 Fox, E. A., Wright, A. E., Fumagalli, M., & Vieira, F. G. (2019). ngsLD: evaluating linkage
 1027 disequilibrium using genotype likelihoods. *Bioinformatics*, 35(19), 3855–3856.
- 1028 Fumagalli, M., Vieira, F. G., Linderoth, T., & Nielsen, R. (2014). ngsTools: methods for
 1029 population genetics analyses from next-generation sequencing data. *Bioinformatics*,
 1030 30(10), 1486–1487.
- 1031 Garcia-Erill, G., & Albrechtsen, A. (2020). Evaluation of model fit of inferred admixture
 1032 proportions. *Molecular Ecology Resources*, 20(4), 936–949.
- 1033 Garrison, E., & Marth, G. (2012). Haplotype-based variant detection from short-read
 1034 sequencing. arXiv. Retrieved from <http://arxiv.org/abs/1207.3907>
- 1035 Gompert, Z., Lucas, L. K., Buerkle, C. A., Forister, M. L., Fordyce, J. A., & Nice, C. C.
 1036 (2014). Admixture and the organization of genetic diversity in a butterfly species
 1037 complex revealed through common and rare genetic variants. *Molecular Ecology*,
 1038 23(18), 4555–4573.
- 1039 Haller, B. C., & Messer, P. W. (2019). SLiM 3: Forward Genetic Simulations Beyond the
 1040 Wright–Fisher Model. *Molecular Biology and Evolution*, 36(3), 632–637.
- 1041 Hill, W. G., & Weir, B. S. (1988). Variances and covariances of squared linkage disequilibria
 1042 in finite populations. *Theoretical Population Biology*, 33(1), 54–78.
- 1043 Holsinger, K. E., Lewis, P. O., & Dey, D. K. (2002). A Bayesian approach to inferring
 1044 population structure from dominant markers. *Molecular Ecology*, 11(7), 1157–1164.
- 1045 Huang, L., Wang, B., Chen, R., Bercovici, S., & Batzoglou, S. (2016). Reveel: large-scale
 1046 population genotyping using low-coverage sequencing data. *Bioinformatics*, 32(11),
 1047 1686–1696.
- 1048 Huang, W., Li, L., Myers, J. R., & Marth, G. T. (2012). ART: a next-generation sequencing
 1049 read simulator. *Bioinformatics*, 28(4), 593–594.
- 1050 Jørsboe, E., & Albrechtsen, A. (2019). A Genotype Likelihood Framework for GWAS with
 1051 Low Depth Sequencing Data from Admixed Individuals. *bioRxiv*. Retrieved from
 1052 <https://www.biorxiv.org/content/10.1101/786384v1.full-text>
- 1053 Kim, S. Y., Lohmueller, K. E., Albrechtsen, A., Li, Y., Korneliussen, T., Tian, G., ... Nielsen,
 1054 R. (2011). Estimation of allele frequency and association mapping using next-
 1055 generation sequencing data. *BMC Bioinformatics*, 12, 231.
- 1056 Korneliussen, T. S., Albrechtsen, A., & Nielsen, R. (2014). ANGSD: Analysis of Next

1057 Generation Sequencing Data. *BMC Bioinformatics*, 15, 356.

1058 Korneliusson, T. S., & Moltke, I. (2015). NgsRelate: a software tool for estimating pairwise
1059 relatedness from next-generation sequencing data. *Bioinformatics*, 31(24), 4009–4011.

1060 Korneliusson, T. S., Moltke, I., Albrechtsen, A., & Nielsen, R. (2013). Calculation of Tajima's
1061 D and other neutrality test statistics from low depth next-generation sequencing data.
1062 *BMC Bioinformatics*, 14, 289.

1063 Kousathanas, A., Leuenberger, C., Link, V., Sell, C., Burger, J., & Wegmann, D. (2017).
1064 Inferring Heterozygosity from Ancient and Low Coverage Genomes. *Genetics*, 205(1),
1065 317–332.

1066 Langmead, B., & Salzberg, S. L. (2013). Langmead. 2013. Bowtie2. *Nature Methods*, 9,
1067 357–359.

1068 Li, H. (2011). A statistical framework for SNP calling, mutation discovery, association
1069 mapping and population genetical parameter estimation from sequencing data.
1070 *Bioinformatics*, 27(21), 2987–2993.

1071 Li, H., Handsaker, B., Wysoker, A., Fennell, T., Ruan, J., Homer, N., ... 1000 Genome
1072 Project Data Processing Subgroup. (2009). The Sequence Alignment/Map format and
1073 SAMtools. *Bioinformatics*, 25(16), 2078–2079.

1074 Li, H., & Ralph, P. (2019). Local PCA Shows How the Effect of Population Structure Differs
1075 Along the Genome. *Genetics*, 211(1), 289–304.

1076 Link, V., Kousathanas, A., Veeramah, K., Sell, C., Scheu, A., & Wegmann, D. (2017).
1077 ATLAS: Analysis Tools for Low-depth and Ancient Samples (p. 105346). doi:
1078 10.1101/105346

1079 Li, R., Li, Y., Fang, X., Yang, H., Wang, J., Kristiansen, K., & Wang, J. (2009). SNP
1080 detection for massively parallel whole-genome resequencing. *Genome Research*, 19(6),
1081 1124–1132.

1082 Liu, S., Huang, S., Chen, F., Zhao, L., Yuan, Y., Francis, S. S., ... Xu, X. (2018). Genomic
1083 Analyses from Non-invasive Prenatal Testing Reveal Genetic Associations, Patterns of
1084 Viral Infections, and Chinese Population History. *Cell*, 175(2), 347–359.e14.

1085 Lorieux, M., Gkanogiannis, A., Fragoso, C., & Rami, J.-F. (2019). NOISYmputer: genotype
1086 imputation in bi-parental populations for noisy low-coverage next-generation sequencing
1087 data (p. 658237). doi: 10.1101/658237

1088 Lucas-Lledó, J. I., Vicente-Salvador, D., Aguado, C., & Cáceres, M. (2014). Population
1089 genetic analysis of bi-allelic structural variants from low-coverage sequence data with
1090 an expectation-maximization algorithm. *BMC Bioinformatics*, 15, 163.

1091 MacConaill, L. E., Burns, R. T., Nag, A., Coleman, H. A., Slevin, M. K., Giorda, K., ...
1092 Thorner, A. R. (2018). Unique, dual-indexed sequencing adapters with UMIs effectively
1093 eliminate index cross-talk and significantly improve sensitivity of massively parallel
1094 sequencing. *BMC Genomics*, 19(1), 30.

1095 Marchini, J., Howie, B., Myers, S., McVean, G., & Donnelly, P. (2007). A new multipoint
1096 method for genome-wide association studies by imputation of genotypes. *Nature
1097 Genetics*, 39(7), 906–913.

1098 Maruki, T., & Lynch, M. (2014). Genome-wide estimation of linkage disequilibrium from
1099 population-level high-throughput sequencing data. *Genetics*, 197(4), 1303–1313.

1100 Maruki, T., & Lynch, M. (2015). Genotype-Frequency Estimation from High-Throughput
1101 Sequencing Data. *Genetics*, 201(2), 473–486.

1102 McKenna, A., Hanna, M., Banks, E., Sivachenko, A., Cibulskis, K., Kernytzky, A., ...
1103 DePristo, M. A. (2010). The Genome Analysis Toolkit: a MapReduce framework for
1104 analyzing next-generation DNA sequencing data. *Genome Research*, 20(9), 1297–
1105 1303.

1106 Meisner, J., & Albrechtsen, A. (2018). Inferring Population Structure and Admixture
1107 Proportions in Low-Depth NGS Data. *Genetics*, 210(2), 719–731.

1108 Money, D., Gardner, K., Migicovsky, Z., Schwaninger, H., Zhong, G.-Y., & Myles, S. (2015).
1109 LinkImpute: Fast and Accurate Genotype Imputation for Nonmodel Organisms. *G3*,
1110 5(11), 2383–2390.

1111 Narasimhan, V., Danecek, P., Scally, A., Xue, Y., Tyler-Smith, C., & Durbin, R. (2016).

- 1112 BCFtools/RoH: a hidden Markov model approach for detecting autozygosity from next-
 1113 generation sequencing data. *Bioinformatics*, 32(11), 1749–1751.
- 1114 Pasaniuc, B., Rohland, N., McLaren, P. J., Garimella, K., Zaitlen, N., Li, H., ... Price, A. L.
 1115 (2012). Extremely low-coverage sequencing and imputation increases power for
 1116 genome-wide association studies. *Nature Genetics*, 44(6), 631–635.
- 1117 Pritchard, J. K., Stephens, M., & Donnelly, P. (2000). Inference of population structure using
 1118 multilocus genotype data. *Genetics*, 155(2), 945–959.
- 1119 Reynolds, J., Weir, B. S., & Cockerham, C. C. (1983). Estimation of the coancestry
 1120 coefficient: basis for a short-term genetic distance. *Genetics*, 105(3), 767–779.
- 1121 Sarmashghi, S., Bohmann, K., P Gilbert, M. T., Bafna, V., & Mirarab, S. (2019). Skmer:
 1122 assembly-free and alignment-free sample identification using genome skims. *Genome
 1123 Biology*, 20(1), 34.
- 1124 Skotte, L., Korneliussen, T. S., & Albrechtsen, A. (2012). Association testing for next-
 1125 generation sequencing data using score statistics. *Genetic Epidemiology*, 36(5), 430–
 1126 437.
- 1127 Skotte, L., Korneliussen, T. S., & Albrechtsen, A. (2013). Estimating individual admixture
 1128 proportions from next generation sequencing data. *Genetics*, 195(3), 693–702.
- 1129 Snyder-Mackler, N., Majoros, W. H., Yuan, M. L., Shaver, A. O., Gordon, J. B., Kopp, G.
 1130 H., ... Tung, J. (2016). Efficient Genome-Wide Sequencing and Low-Coverage
 1131 Pedigree Analysis from Noninvasively Collected Samples. *Genetics*, 203(2), 699–714.
- 1132 Stapley, J., Feulner, P. G. D., Johnston, S. E., Santure, A. W., & Smadja, C. M. (2017).
 1133 Variation in recombination frequency and distribution across eukaryotes: patterns and
 1134 processes. *Philosophical Transactions of the Royal Society of London. Series B,
 1135 Biological Sciences*, 372(1736). doi: 10.1098/rstb.2016.0455
- 1136 Tang, H., Peng, J., Wang, P., & Risch, N. J. (2005). Estimation of individual admixture:
 1137 analytical and study design considerations. *Genetic Epidemiology*, 28(4), 289–301.
- 1138 Van Belleghem, S. M., Rastas, P., Papanicolaou, A., Martin, S. H., Arias, C. F., Supple, M.
 1139 A., ... Papa, R. (2017). Complex modular architecture around a simple toolkit of wing
 1140 pattern genes. *Nature Ecology & Evolution*, 1(3), 52.
- 1141 Vieira, F. G., Albrechtsen, A., & Nielsen, R. (2016). Estimating IBD tracts from low coverage
 1142 NGS data. *Bioinformatics*, 32(14), 2096–2102.
- 1143 Vieira, F. G., Fumagalli, M., Albrechtsen, A., & Nielsen, R. (2013). Estimating inbreeding
 1144 coefficients from NGS data: Impact on genotype calling and allele frequency estimation.
 1145 *Genome Research*, 23(11), 1852–1861.
- 1146 Vieira, F. G., Lassalle, F., Korneliussen, T. S., & Fumagalli, M. (2016). Improving the
 1147 estimation of genetic distances from Next-Generation Sequencing data. *Biological
 1148 Journal of the Linnean Society. Linnean Society of London*, 117(1), 139–149.
- 1149 Wasik, K., Berisa, T., Pickrell, J. K., Li, J. H., Fraser, D. J., King, K., & Cox, C. (2019).
 1150 Comparing low-pass sequencing and genotyping for trait mapping in pharmacogenetics
 1151 (p. 632141). doi: 10.1101/632141
- 1152 Whalen, A., Gorjanc, G., & Hickey, J. M. (2019). Parentage assignment with genotyping-by-
 1153 sequencing data. *Journal of Animal Breeding and Genetics = Zeitschrift Fur
 1154 Tierzucht Und Zuchtungsbiologie*, 136(2), 102–112.

1155